

# A Deep Learning Approach to Quasar Continuum Prediction

Bin Liu,<sup>1</sup><sup>★</sup> Rongmon Bordoloi,<sup>1</sup><sup>†</sup>

<sup>1</sup>*Department Of Physics, North Carolina State University, Raleigh, North Carolina, 27695*

Accepted —. Received —; in original form —

## ABSTRACT

We present a novel deep learning model, intelligent quasar continuum neural network (iQNet), which predicts the intrinsic continuum of any quasar in the rest-frame wavelength range  $1020\text{\AA} \leq \lambda_{\text{rest}} \leq 1600\text{\AA}$ . We train this network using high-resolution Hubble Space Telescope/Cosmic Origin Spectrograph ultraviolet quasar spectra at low redshift ( $z \sim 0.2$ ) from the Hubble Spectroscopic Legacy Archive (HSLA), and apply it to predict quasar continua from different astronomical surveys. We utilize the HSLA quasar spectra that are well-defined in the rest frame wavelength range  $[1020, 1600]\text{\AA}$  with an overall median signal-to-noise ratio of at least five. In addition, we introduce a standardization process to the data, which reduces the absolute fractional flux error (AFFE) of the predicted continua approximately by half. To create a training set for our neural network, we use principal component analysis (PCA) and Gaussian mixture model (GMM) to classify the HSLA quasar spectra into four classes and use them to synthesize mock quasar spectra to increase the size of training data set. iQNet achieves a median AFFE of 1.31% on the training quasar spectra, which is approximately ten times better than traditional PCA-based prediction methods, and 4.17% on the testing quasar spectra. We apply iQNet and predict the continua of  $\sim 3200$  SDSS-DR16 quasar spectra at higher redshift ( $2 < z \leq 5$ ) and measure the redshift evolution of mean transmitted flux ( $\langle F \rangle$ ) in the Ly- $\alpha$  forest region. We measure a gradual evolution of  $\langle F \rangle$  with redshift, which we characterize as a power-law fit to the effective optical depth of the Ly- $\alpha$  forest. Our measurements are broadly consistent with other estimates of  $\langle F \rangle$  in the literature but provide a more accurate measurement as we are directly measuring the quasar continuum where there is minimum contamination from the Ly- $\alpha$  forest. This work proves that the deep learning iQNet model can predict the quasar continuum with high accuracy and shows the viability of such methods for quasar continuum prediction.

**Key words:** (galaxies:) intergalactic medium, (galaxies:) quasars: absorption lines, machine learning, lyman- $\alpha$  forest

## 1 INTRODUCTION

The Ly- $\alpha$  forest absorption in the spectra of high redshift objects is imprinted by neutral hydrogen in the intergalactic medium (IGM), which makes up most of the baryons in the early Universe (Shull 2014). This is unlike lower redshifts, where a significant fraction of the baryons reside in the circumgalactic medium of galaxies (Tumlinson et al. 2013; Werk et al. 2014; Bordoloi et al. 2014; Chen et al. 2018). Our understanding of the Ly- $\alpha$  forest changed dramatically in the late 1990s when the pioneering hydrodynamical simulations showed that the Ly- $\alpha$  forest statistics could be understood if the neutral gas followed the underlying dark matter distribution in the cosmic web of filaments, voids, and clusters (Cen et al. 1994; Hernquist et al. 1996; Croft et al. 1998). The properties of the Ly- $\alpha$  forest inform us about the density, temperature, and ionization state

of the IGM. Subsequently, both the 1-D power spectrum of HI column density, and the evolution of the mean transmitted flux in the Ly- $\alpha$  forest along the lines of sight to distance quasars are studied for a small sample of bright high-resolution quasar spectra (Rauch et al. 1997; Schaye et al. 2003; Songaila 2004; Kirkman et al. 2005; Becker et al. 2010; Faucher-Giguère et al. 2008), and large samples of moderate resolution SDSS spectra (Bernardi et al. 2003; McDonald et al. 2005; Pâris et al. 2011; Lee et al. 2012; Becker et al. 2013; Davies et al. 2018).

One of the basic observable used to quantify flux distribution in the Ly- $\alpha$  forest is the evolution of mean transmitted flux,  $\langle F \rangle$ , with redshift (e.g. Faucher-Giguère et al. 2008; Becker et al. 2010). The effective optical depth,  $\tau_{\text{eff}}$ , of the Ly- $\alpha$  forest ( $\tau_{\text{eff}} = -\ln \langle F \rangle$ ) can be used to constrain the metagalactic ionizing background intensity (Rauch et al. 1997; Bolton et al. 2005; McDonald et al. 2005; McDonald et al. 2001; Becker et al. 2013). The transmitted flux  $F$  for any arbitrary quasar spectrum is defined as

<sup>★</sup> Email: bliu8@ncsu.edu

<sup>†</sup> Email: rbordol@ncsu.edu

$$F = \frac{F_{\text{spec}}}{F_{\text{cont}}}, \quad (1)$$

where  $F_{\text{spec}}$  is the observed quasar flux in its rest frame, and  $F_{\text{cont}}$  is the true quasar continuum without any absorption.

To study the properties of the Ly- $\alpha$  forest, we need to know the true quasar continuum ( $F_{\text{cont}}$ , equation 1) to make correct estimates of  $\langle F \rangle$  and therefore  $\tau_{\text{eff}}$ . The uncertainty in predicting the true continuum is often one of the largest uncertainties in studying the IGM (e.g. Croft et al. 2002). Thus, an accurate model to predict the quasar continuum in the presence of Ly- $\alpha$  forest absorption is necessary for scientists to study neutral hydrogen in the IGM.

Previous studies have defined the transmission peaks in the Ly- $\alpha$  forest region as the continuum in high redshift quasars using high resolution-echelle spectra (e.g. Rauch et al. 1997; Schaye et al. 2003). However, cosmic voids along the line of sight have sufficient optical depth to bias such measurements in underestimating the true continuum. This can be corrected statistically by using synthetic spectra from hydrodynamical simulations (Faucher-Giguère et al. 2008). Unfortunately, such correction also relies on the veracity of the simulations/models themselves and is not, in fact, a direct measurement of  $\tau_{\text{eff}}$ .

Other studies used a large number of moderate-resolution spectra to either statistically correct for the continuum (Bernardi et al. 2003), used composite spectra of  $z > 2$  quasars to statistically study the evolution of  $\tau_{\text{eff}}$  (Becker et al. 2013), or used principal component analysis (PCA) of  $z \sim 3$  quasars to predict the true continuum (Pâris et al. 2011). Composite spectra can be used to estimate very robust "differential"  $\tau_{\text{eff}}$  evolution from the stacked spectra in different redshift bins. However, this method relies on two assumptions: (1) all stacked quasar spectra have the same "shape", and (2) the true quasar continuum can be represented by the composite spectra at  $z \sim 2.15$ . Both these assumptions may not be always very accurate.

PCA-based prediction models are popular due to the rise of machine learning applications, (e.g. Suzuki et al. 2005; Pâris et al. 2011; Lee et al. 2012; Davies et al. 2018). However, the main drawback of this type of model is its limited generalizability. A PCA prediction model usually consists of two sets of principal components, which recover the full wavelength coverage of the quasar continuum and the part of the quasar continuum redward of quasar Ly- $\alpha$  emission, respectively. Further, a transformation matrix is used to transform the PCA weights of continuum redward of Ly- $\alpha$  emission into the weights of the whole continuum. PCA reconstruction models are usually required to recover over 97.5% of the variance of the flux within the wavelength of interest. However, there are no studies to evaluate the correlations between the reconstruction ratios of the weights of those two sets of principal components.

Another important step in evaluating the performance of a PCA model is to use an independent testing data set that should never be used for training and only reserved to test and evaluate the researched model. Evaluating the model accuracy based on a training data set only reflects how well it performs through the training process but does not reflect how well it will work on a testing data set. Because the model has been constructed based on the information extracted from the training data set, the model will, unsurprisingly, perform well on the training data. All of the published PCA models used for quasar continuum estimation use the same data set to both train the weights of the PCA models and test the performance of those models. Therefore, the robustness of PCA models on a testing data set is never known if the performance of researched models is evaluated on a training data set. A robust model needs to be tested

so that it performs well not only on the training data but also on the testing data that have never been exposed to the model. The testing data set will be the model benchmark to make sure that the model generalizes well and robustly on the unseen data.

Moreover, all studies either indirectly measure  $\tau_{\text{eff}}$  using simulations or models (Faucher-Giguère et al. 2008), or use  $z \sim 2$  quasar spectra as the ground truth continuum. To overcome this shortcoming, and to better predict the true quasar continuum uncontaminated by Ly- $\alpha$  forest at high redshift, in this paper, we employ  $z < 1$  quasar spectra observed with Hubble Space Telescope's Cosmic Origin Spectrograph (HST/COS). We develop a novel deep learning approach using quasar spectra at low redshift ( $z < 1$ ) where the spectra are least affected by the Ly- $\alpha$  forest and predict quasar continua at higher redshift ( $2 < z \leq 5$ ). This method allows us to compute  $\tau_{\text{eff}}$  by predicting the true quasar continuum at high redshift over the range  $2 < z_{\text{QSO}} \leq 5$  directly, and to test the performance of our model by using a testing data set that is never used during the training phase on the quasar continuum model.

This paper is organized as follows: in Section 2, we present the quasar spectra used in this work from Hubble Spectroscopic Legacy Archive and Sloan Digital Sky Survey, respectively. In Section 3, we construct our deep neural network, iQNet, and apply a standardization process and present the use of principal component analysis. In Section 4, we compute the absolute fractional flux error and use it as a goodness of fit to evaluate the model performance among iQNet and PCA prediction models. We measure the evolution of the mean transmitted flux in the Ly- $\alpha$  forest with redshift and compare our findings with literature measurements in Section 4.4. Throughout this work, we adopted a  $\Lambda$ CDM cosmology ( $\Omega_m = 0.286$ ,  $\Omega_\Lambda = 0.71$ ,  $H_0 = 69.32 \text{ km s}^{-1} \text{ Mpc}^{-1}$ ,  $\Omega_b = 0.04628$ ), from the Wilkinson Microwave Anisotropy Probe nine-year data (Hinshaw et al. 2013).

## 2 DESCRIPTION OF OBSERVATIONS

### 2.1 Quasar Spectra from the Hubble Spectroscopic Legacy Archive (HSLA)

We use the UV quasar spectra from the Hubble Spectroscopic Legacy Archive Data Release 2 (Peeples et al. 2017) in this research. This data set contains 799 unique quasar spectra, with mean redshift  $\langle z_{\text{QSO}} \rangle = 0.689$ . The data set comprises of 542, 326, 197 HST/COS (Green et al. 2011) spectra observed with the G130M, G160M, G140L far-UV gratings, 43, 23, and 15 HST/COS spectra observed with the G230L, G185M, and G225M near-UV gratings, respectively. We cross-match HST/COS quasars with the Million Quasars Catalog (Flesch 2019) to obtain the quasar redshifts. We select the HST-COS quasars that fully cover the rest-frame wavelength range of  $1020\text{\AA} \leq \lambda_{\text{rest}} \leq 1600\text{\AA}$  and have a median signal to noise ratio  $(S/N) > 5$  per resolution element. These selection criteria yield 63 quasars with  $z_{\text{QSO}} < 1$ . The left panel in Figure 1 shows the redshift distribution of these selected quasars from the HSLA. We bin each HST-COS spectrum to Nyquist sampling with three pixels per COS resolution element (FWHM  $\sim 18 \text{ km/s}$ ). We shift each quasar spectrum to its rest frame, and re-sample it on a uniform wavelength grid of  $0.05\text{\AA}$  per pixel, which is approximately the mean resolution of those 63 selected quasar spectra. We compute the relative flux of each quasar spectrum by dividing the flux by the average flux of 40 pixels centered at  $1280\text{\AA}$ . Throughout the paper, we will use this relative flux to predict the shape of the quasar continuum.

To create the ground truth for a deep learning interface, we

first need to identify the continuum for each of these  $z < 1$  quasars. We perform this task using the interactive continuum fitting tool, Lintools API<sup>1</sup>. We fit a quasar continuum for each quasar spectrum by masking out all the absorption lines and locally fitting a spline curve to trace the strong emission lines of OVI, Ly- $\alpha$ , SiIV, NV, and CIV. We use these quasar continua as the ground truth and they are used to test the robustness of our fitting procedures. We randomly select 85% of the 63 fitted continua and their corresponding quasar spectra to form the training data set. We treat the remaining 15% of the sample as the testing data, which are not used in the training phase of neural network and only reserved for performance evaluation of the researched models.

## 2.2 Quasar Spectra from Sloan Digital Sky Survey (SDSS)

The Sloan Digital Sky Survey Data Release 16 contains optical spectroscopy of more than 750,000 unique quasars (Ahumada et al. 2019; Higley et al. 2020). We proceed to use these observations to predict the quasar continua at different redshifts based on the continua obtained from the low redshift HSLA data. To that end, we randomly select 5000 quasar spectra through the SDSS SkyServer<sup>2</sup> that satisfy the following criteria:

- Median signal-to-noise ratio  $S/N > 5$  per pixel
- QSO redshifts  $2.0 \leq z_{\text{QSO}} \leq 5.0$
- Minimum rest-frame wavelength  $\lambda_{\text{min}} \geq 1080\text{\AA}$

We visually verify the downloaded quasar spectra and further discard spectra that are misclassified as quasars or have a bad  $z_{\text{QSO}}$ . This leaves us a final sample of 3196 spectra. The right panel of Figure 1 shows the redshift distribution of these quasars. The quasars continuously cover the redshift range between  $z_{\text{QSO}} = 2.3$  and  $z_{\text{QSO}} = 5.1$  with the mean value of  $\langle z_{\text{QSO}} \rangle = 3.5$ . We will use these SDSS quasar spectra to study the evolution of the mean effective optical depth in Section 3.5.

We transform the quasar spectra into their rest frame and re-sample them onto a uniform wavelength grid. Each spectrum flux is then re-normalized with the mean flux at  $\sim 1218\text{\AA}$ . We are interested in predicting the rest frame quasar continuum within the wavelength range  $[1020, 1600]\text{\AA}$ , therefore for all the SDSS spectra, only the flux in that wavelength range is retained for further analysis.

## 3 METHODS

### 3.1 intelligent Quasar Continuum Neural Network (iQNet)

Deep neural networks have a proven track record for image restoration and image synthesis (Zhou et al. 1988). In this work, we show how deep neural networks can be applied to successfully predict quasar continuum at any redshift. We treat a 1-D rest-frame UV quasar spectrum as a 1-D image array. Each input quasar spectrum to this network is a superposition of the true quasar continuum, random noise owing to finite signal-to-noise ratio, and intervening HI and metal absorption line systems that are imprinted on the quasar spectra along the line of sight. Instead of building a more advanced architecture (i.e., the Variational Autoencoder (VAE) and the Generative Adversarial Network (GAN)), we start with the simpler autoencoder (AE) architecture. Occam's razor in deep learning suggests that it is not necessary to apply a complicated network



**Figure 1.** Redshift distributions of the selected quasars from HSLA (blue) and SDSS DR16 (red), respectively. We utilize 63 quasars from HSLA and 3,196 quasars from SDSS DR16 to train and test the performance of iQNet.

structure if the simpler network is able to solve the problem. The inspiration for our deep neural network architecture is analogous to the idea of the stacked denoising autoencoder (e.g. Vincent et al. 2010). However, the structure shapes of the encoder and decoder are not symmetric to the coding layer. Our deep neural network, iQNet, will take the part of the quasar spectrum redward of the Ly- $\alpha$  line ( $[1216, 1600]\text{\AA}$ ) as input and generate the whole ( $[1020, 1600]\text{\AA}$ ) quasar continuum as output.

The architecture of our intelligent quasar Continuum Neural Network, (iQNet) is shown in Table 1. The iQNet is compiled and trained using the Keras<sup>3</sup> with Tensorflow<sup>4</sup> backend, (e.g. Chollet et al. 2015; Abadi et al. 2015). To utilize the power of denoising autoencoder, we treat the quasar spectra redward of Ly- $\alpha$  emission as a superposition of ground truth continua, random noise, and intervening absorption line systems imprinted on the spectra. The objective of the neural network is to discover the underlying ground truth continua, despite the presence of noise and absorption lines. The iQNet network takes a 1-D quasar spectrum in the rest-frame redward wavelength range  $1216\text{\AA} \leq \lambda_{\text{rest}} \leq 1600\text{\AA}$  as input and generates the corresponding quasar continuum in the full wavelength range of interest ( $1020\text{\AA} \leq \lambda_{\text{rest}} \leq 1600\text{\AA}$ ). The loss function to optimize our neural network is binary cross-entropy with Adam optimization (Kingma & Ba 2014) and a training batch size of 512 quasar spectra redward of Ly- $\alpha$  emission from the training set. The order of training spectra is also randomly shuffled every epoch (training cycle) before they are fed into our neural network to reduce the training bias. To quantify the performance of our neural network model and the goodness of fit, we use the absolute fractional flux error (AFFE) to evaluate our model to make sure that the weights of the iQNet are updated to achieve a lower AFFE and reach to the minimum of the loss function at the same time. We define the absolute fractional flux error,  $|\delta F|$ , as

$$|\delta F| = \int_{\lambda_1}^{\lambda_2} \left| \frac{F_{\text{pred}}(\lambda) - F_{\text{true}}(\lambda)}{F_{\text{true}}(\lambda)} \right| d\lambda \bigg/ \int_{\lambda_1}^{\lambda_2} d\lambda \quad (2)$$

where  $F_{\text{pred}}$  is the predicted continuum and  $F_{\text{true}}$  is the true continuum. An Early Stopping (Prechelt 1996) strategy is also used to terminate the training process if there is no weight update available.

<sup>1</sup> <https://lintools.readthedocs.io>

<sup>2</sup> <http://skyserver.sdss.org/dr16/en/tools/search/sql.asp>

<sup>3</sup> <https://keras.io/>

<sup>4</sup> <https://www.tensorflow.org/>

**Table 1.** intelligent Quasar Continuum Neural Network (iQNet) Architecture. The FC layers represent neural layers with all fully-connected neurons. The ELU activation function represents the exponential linear unit function.

Layer Type	Number of Neurons	Activation Function
Input Layer	7680	N/A
FC Layer	1024	ELU
FC Layer	512	ELU
FC Layer	256	ELU
FC Layer	256	ELU
FC Layer	512	ELU
FC Layer	1024	ELU
FC Layer	2048	ELU
Output Layer	11600	Sigmoid

We also add a median filter of the size of 50 pixels to smooth out the output continuum. The size of the median filter is a hyper-parameter and we have tested that a median filter of 50 pixels provides the lowest AFPE among filter size range from 0 to 100 pixels with a 10-pixel increment.

### 3.2 Standardization Process

To avoid model over-fitting and reduce model bias, we add a pre-processing step prior to model training called standardization. The standardization process is defined as

$$f_{\text{input}} = \frac{f - f_{\min}}{f_{\max} - f_{\min}} \quad (3)$$

where  $f_{\text{input}}$  is the scaled flux used as model input after the standardization process,  $f$  is the original relative flux,  $f_{\max}$  is the maximum value of quasar flux in the training spectra, and  $f_{\min}$  is the minimum flux in the training spectra. This process applies to the individual relative flux of each quasar spectrum or continuum in both the training and testing data sets. After this transformation, all quasar scaled fluxes should be within the range  $[0, 1]$ . We apply this transformation to scale down the dominant Ly- $\alpha$  and CIV emissions and to un-correlate the emission features in quasar spectra.

In addition, we define the corresponding inverse transformation of standardization as

$$f_{\text{pred}} = f_{\text{output}} \cdot (f_{\max} - f_{\min}) + f_{\min} \quad (4)$$

where  $f_{\text{output}}$  is the scaled flux output from the prediction model and  $f_{\text{pred}}$  is the predicted relative flux after the inverse transformation of this standardization process. Hence, the standardization process and its inverse transformation are internal processes added to the prediction model and have no physical meaning for quasar study.

### 3.3 Principal Component Analysis (PCA)

We have only a limited number of training quasar spectra available from HSLA (53 quasars) that meet our wavelength coverage and S/N cutoff requirements. Therefore to increase the number of training spectra, we need to synthesize mock 1-D quasar spectra using the selected training continua.

The training spectra cover  $[1020, 1600]\text{\AA}$  with  $0.05\text{\AA}$  per pixel; i.e., there are 11,600 pixels for each quasar spectrum). To reduce the computational complexity, we apply the Principal Component Anal-

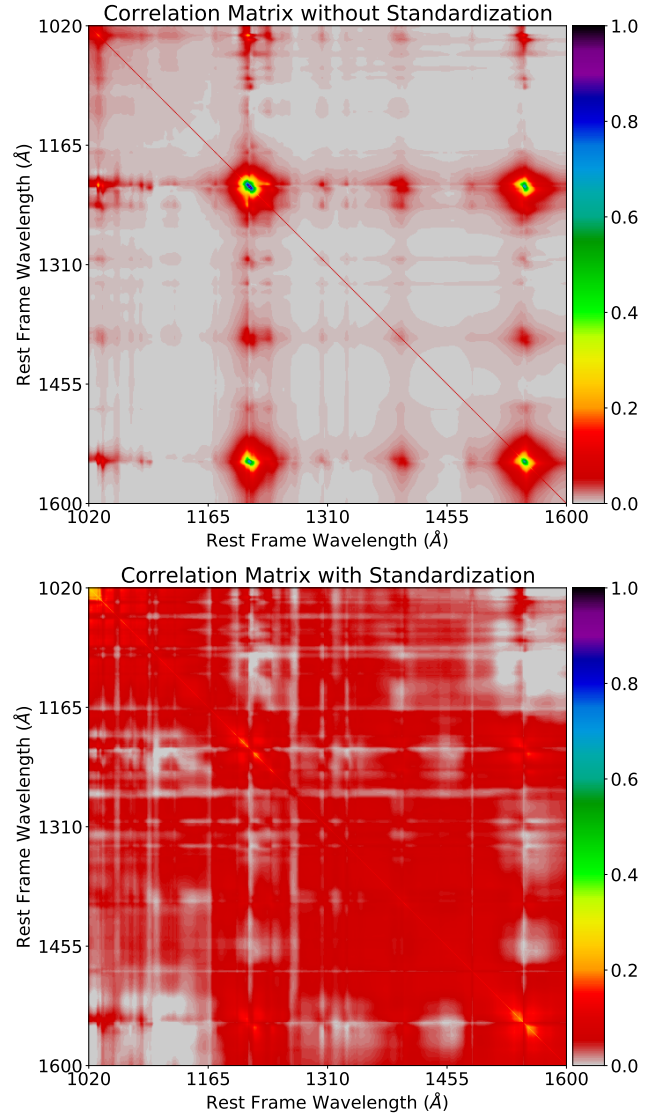


**Figure 2.** Difference between correlation matrices with and without standardization. Top panel shows strong correlations at Ly- $\alpha$  and CIV transitions indicating that these two features are positively correlated and introduce bias to the PCA model without standardization. Bottom panel illustrates no strong correlation shows up with the addition of standardization process prior to PCA construction, indicating that the PCA model with standardization is not biased from the dominant Ly- $\alpha$  and CIV features. The color bar in both panels illustrates the correlation coefficients within the rest-frame wavelength range  $1020\text{\AA} \leq \lambda_{\text{rest}} \leq 1600\text{\AA}$

ysis<sup>5</sup> by Buitinck et al. (2013) (PCA) as a dimensionality reduction tool to reduce the 11,600 data points on each quasar spectrum to a small number of principal components that can reconstruct 97.5% of spectral flux of the training HSLA quasar continua.

We perform two sets of PCA decomposition, both with and without the standardization process described in Section 3.2. After the PCA model construction, we are able to compute the correlation matrix using PCA models to demonstrate the data correlation. The

<sup>5</sup> <https://scikit-learn.org/stable/modules/generated/sklearn.decomposition.PCA.html>

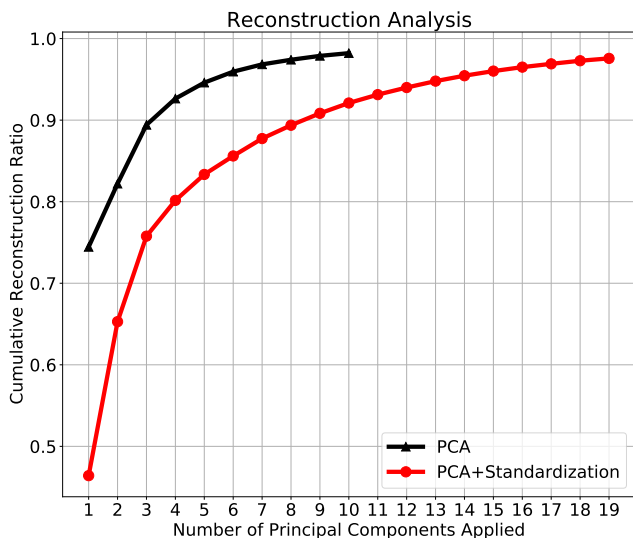


**Figure 3.** PCA reconstruction ratio is also known as the explained variance ratio. The cumulative reconstruction ratio tells how much percentage the PCA recovers the original training continua with an increasing number of principal components up to 97.5% of original training quasar continua. The PCA model without standardization requires 10 principal components because it is biased by the dominant Ly- $\alpha$  and CIV correlated features. The PCA model with the standardization process needs 19 principal components because the standardization properly scales down and un-correlates the Ly- $\alpha$  and CIV features.

top panel of Figure 2 shows that there are strong correlations at Ly- $\alpha$  and CIV emissions. In other words, this PCA model is biased by the strong Ly- $\alpha$  and CIV emissions. For the PCA model without the standardization process, Figure 3 illustrates that it only requires 10 principal components to reconstruct 97.5% of the training spectra because it captures the dominant emission features and ignores other weak features to represent a quasar continuum.

The PCA model with the added standardization process requires 19 principal components to reconstruct 97.5% of the training quasar continua. The bottom panel in Figure 2 shows that there is no correlation coefficient greater than 0.4. This illustrates that all features in the training data set have been uncorrelated prior to PCA model construction by the standardization process. Figure 3 demonstrates the cumulative reconstruction ratio with the number of principal components for the PCA model with the added standardization process. The first 10 principal components of this PCA model can reconstruct ~92% of the original quasar continua. To achieve our goal of 97.5% reconstruction of the original spectra, we use 19 PCA components.

Our PCA model predicts the rest-frame UV quasar continuum in the wavelength range  $1020\text{\AA} \leq \lambda_{\text{rest}} \leq 1600\text{\AA}$ . Even though this PCA+Standardization model needs the additional 9 components, the bottom panel of Figure 2 shows there is no strong correlation after the standardization process. This means that there are no dominant features biased to the PCA model with standardization. We prefer the PCA model with the addition of the standardization process because the AFFE (see Section 4.1) for a PCA model with standardization is much lower than that of the PCA model without standardization. A lower AFFE indicates that the PCA reconstruction is closer to the original quasar spectra. Therefore, the standardization process is necessary for PCA construction.

We note that, while we apply the Principal Component Anal-

ysis to reduce the computational complexity, others have proved that PCA can be used to predict quasar continua as a prediction model. Suzuki et al. (2005), Pâris et al. (2011) obtain such PCA prediction models by constructing two PCA models, one covering the rest-frame wavelength range ( $[1020, 1600]\text{\AA}$ ) and the other covering the part of the spectra redward of the Ly- $\alpha$  line ( $[1216, 1600]\text{\AA}$ ). They further use a transformation matrix, which converts the weights of principal components in the eigenspace covering the continuum redward of Ly- $\alpha$  into the weights in the eigenspace that covers the whole continuum. Both of these approaches do not utilize the standardization approach introduced here. We follow the same procedure discussed in Suzuki et al. (2005) and compare the results in Section 4 to demonstrate the limited generalization ability of the PCA prediction model.

### 3.4 Generation of Synthetic Quasar Spectra

To augment our training set, we proceed to create a large number of synthetic quasar spectra as described below. To create a representative training set, we first have to identify how many different classes of quasar continua are present in the training set. To estimate this, we apply the Gaussian mixture model<sup>6</sup> (GMM, Reynolds 2009) clustering algorithm to classify the training quasar continua into different classes. To reduce the computational complexity, we apply the PCA with standardization and use 19 principal components as the input to the GMM model instead of the original quasar spectra.

To determine the correct number of quasar classifications of the training data set and quantify the goodness of clustering, we construct 19 GMM models with the pre-defined class numbers ranging from 2 classes to 20 classes and compute the Bayesian Information Criterion (BIC) (Schwarz 1978) and the Calinski-Harabasz Index (Caliński & Harabasz 1974), as shown in Figure 4. Both Bayesian Information Criterion and Calinski-Harabasz Index are common metrics used for model selection in the clustering algorithm, like GMM, to determine the best model among the available candidates in machine learning. A lower BIC score indicates a better clustering model. Therefore, the GMM results with 2, 3, 4, and 5 classes provide the same clustering goodness given the training data set based on the BIC score, and we need an additional metric, the Calinski-Harabasz Index, to further determine the best clustering number among 2, 3, 4, and 5 classes. We are able to apply the Calinski-Harabasz Index to the training data because the correct number of quasar classes is unknown. The higher the Calinski-Harabasz Index score, the better the GMM model predicts the clusters given a pre-selected number of clusters. The bottom panel in Figure 4 shows the highest Calinski-Harabasz Index is at 4-class clustering GMM model. Thus, 4 classes provide the best clustering result based on the GMM clustering algorithm.

The top panel of Figure 5 shows the mean quasar spectrum obtained by averaging the 63 HSLA quasar spectra selected for this work. All these spectra completely cover the wavelength range of  $1020\text{\AA} \leq \lambda_{\text{rest}} \leq 1600\text{\AA}$ . Prominent emission features, such as Ly- $\alpha$ , CIV, Ly- $\beta$ , OVI, and SiIV, are observed and marked with vertical dotted lines. The horizontal dashed line shows the approximate power law continuum of this composite quasar spectrum. The four classes of spectra identified are essentially a decomposition of this mean quasar spectrum. Figure 5, bottom presents the mean quasar

<sup>6</sup> <https://scikit-learn.org/stable/modules/generated/sklearn.mixture.GaussianMixture.html>



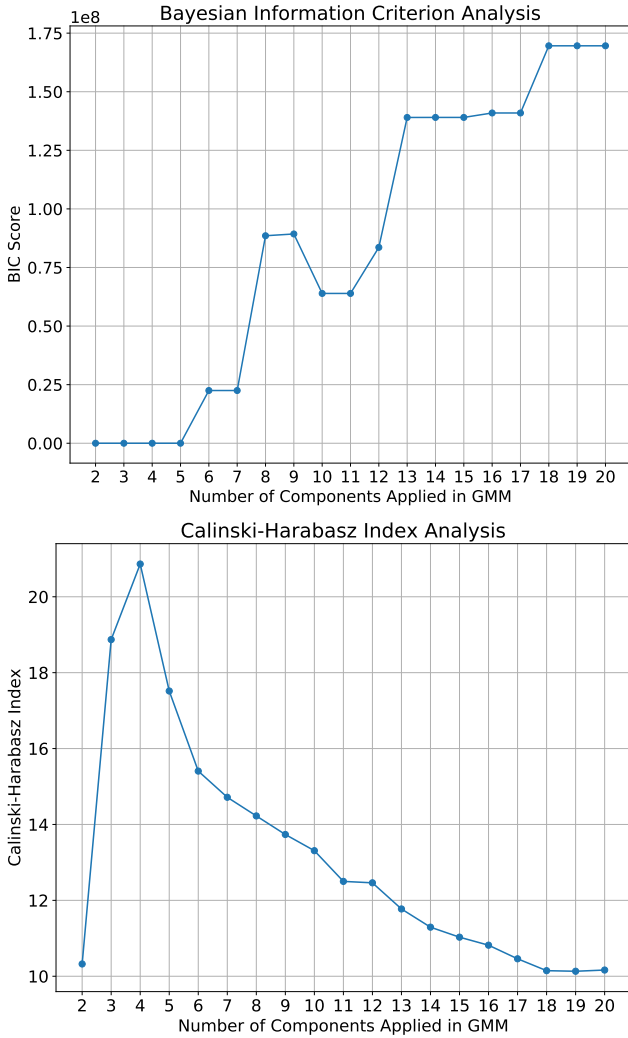


**Figure 4.** Bayesian Information Criterion (BIC) Scores and Calinski-Harabasz Index Scores from 2 Classes to 20 Classes. The numbers of quasar classes, 2, 3, 4, and 5, all provide the lowest BIC scores, indicating that those numbers of classes are representative numbers in the GMM clustering analysis. Four quasar classes in the Calinski-Harabasz Index Analysis illustrate the highest score, indicating that four classes are the best number of quasar classes pre-set to the GMM model.

spectra from all four classes. The primary difference among different quasar classes is particularly seen in the variation of Ly- $\alpha$  and CIV emission strengths. Additionally, we see secondary differences as small variations in the slope of the continua blueward of Ly- $\alpha$  emission. In addition to those four types of quasar spectra, we add the fifth quasar class with a constant relative flux of 1 representing a BL-Lac like AGN spectra, which is not well represented in our training spectra.

We use these five classes of quasar spectra to generate mock spectra to augment our training set. The mock quasar spectra are synthesized with the following steps:

- randomly selecting a quasar continuum from one of the five quasar classes,
- shifting the quasar to a higher redshift ( $z_{QSO}$ ),
- injecting Voigt profiles of a random column density of strong

ISM and HI absorption lines for the Milky Way and at higher random absorber redshift ( $z_{abs} \leq z_{QSO}$ ),

- adding Gaussian noise to the spectra with S/N = 5, 10, and 20.

We maintain the same number of mock quasar spectra in each class such that the neural network is not biased on a specific class of quasar spectra during the training phase. We finally have  $\sim 12,000$  training spectra, including real HSLA quasar spectra and synthesized mock spectra. We train the iQNet model on these 12,000 mock + real HSLA quasar spectra in the Google Colab<sup>7</sup> environment with GPU acceleration enabled for the maximum time of 40 min or an EarlyStopping condition is satisfied.

### 3.5 Mean Transmitted Flux Estimate

We now use our iQNet predicted continua at higher redshift to estimate the evolution of mean transmitted flux in the Ly- $\alpha$  forest with redshift. The mean transmitted flux in the Ly- $\alpha$  forest can be defined as follows:

If  $F_{\text{spec}}$  and  $F_{\text{cont}}$  are the relative flux (normalized to average flux at 1218 Å) and the corresponding continuum as a function of the observed wavelength (e.g. Faucherâ&Gigluâ&Alre et al. 2008), respectively, then the corresponding redshift of Ly- $\alpha$  transition along the line of sight is  $z_{\text{Ly-}\alpha} = \lambda/\lambda_{\text{Ly-}\alpha} - 1$ , where  $\lambda_{\text{Ly-}\alpha} = 1215.67\text{Å}$ . The transmitted flux  $F(z_{\text{Ly-}\alpha})$  as a function of Ly- $\alpha$  redshift  $z_{\text{Ly-}\alpha}$  is:

$$F(z_{\text{Ly-}\alpha}) = \frac{F_{\text{spec}}(z_{\text{Ly-}\alpha})}{F_{\text{cont}}(z_{\text{Ly-}\alpha})}. \quad (5)$$

The mean transmitted flux  $\langle F(z_{\text{Ly-}\alpha}) \rangle$  is the ensemble average of  $F(z_{\text{Ly-}\alpha})$  within a redshift bin, in the Ly- $\alpha$  forest region.

We follow a method similar to the one outlined in Faucherâ&Gigluâ&Alre et al. (2008) to compute  $F(z_{\text{Ly-}\alpha})$ , and we summarize below:

- Extract the quasar spectrum and its corresponding predicted continuum in the Ly- $\alpha$  forest region and calculate its transmitted flux  $F(z_{\text{Ly-}\alpha})$  using Equation 5.
- Mask out the flux regions near the quasar proximity zone (Faucherâ&Gigluâ&Alre et al. 2008). Here, we masked out any points that are within 25 proper Mpc of the quasar redshift. Following Faucherâ&Gigluâ&Alre et al. (2008), the typical size of HI-ionizing radiation of quasars is approximately  $\sim 5$  proper Mpc, thus there should be little contamination left after we mask out the 25 proper Mpc.
- Re-sample all pixels in the Ly- $\alpha$  forest regions in 3 proper Mpc intervals. We bin all pixels in 3 proper Mpc intervals to un-correlate the values of the optical depth in the Ly- $\alpha$  forest region and make them independent of their neighbors. (Faucherâ&Gigluâ&Alre et al. 2008).
- Divide the Ly- $\alpha$  forest region into 30 redshift bins with  $\Delta z_{\text{Ly-}\alpha} = 0.1$ .
- Within each redshift bin, we define the mean transmitted flux ( $\langle F(z_{\text{Ly-}\alpha}) \rangle$ ) as the 3-sigma-clipped mean of the distribution, and convert into the effective optical depth ( $\tau_{\text{eff}} = -\ln\langle F \rangle$ ). Sigma clipping is used to account for any bad pixels or other contamination that might be present in each bin.
- We estimate uncertainty on  $\langle F(z_{\text{Ly-}\alpha}) \rangle$  estimates using a bootstrap with replacement approach. In each redshift bin, we re-sample

<sup>7</sup> colab.research.google.com

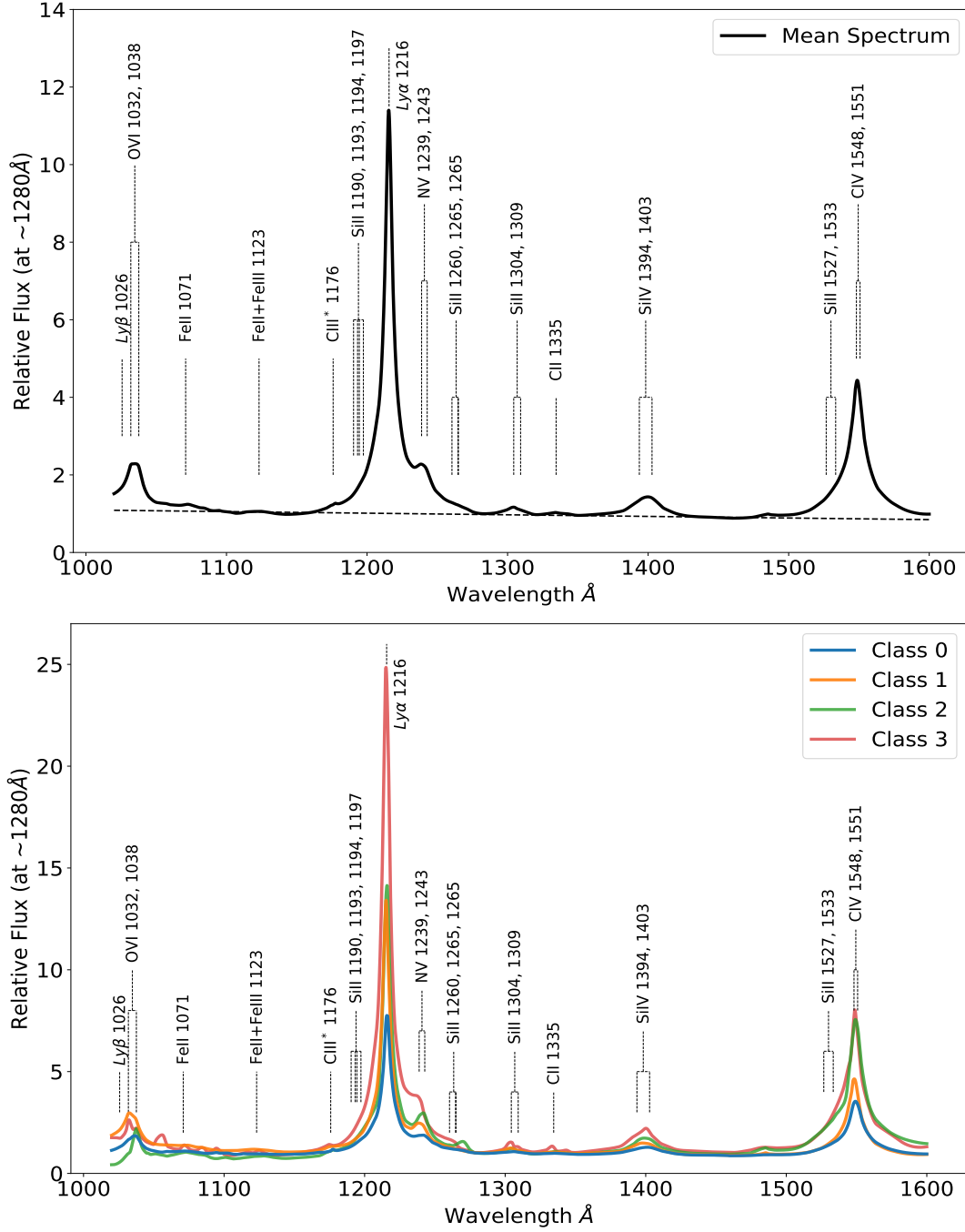


**Figure 5.** *Top Panel:* Mean quasar spectrum obtained from the 63 ( $z \sim 0.2$ ) quasars observed with high resolution HST/COS spectroscopy covering the full rest-frame wavelength range of  $1020\text{\AA} \leq \lambda_{\text{rest}} \leq 1600\text{\AA}$ . Prominent emission features are marked with vertical dashed lines. The spectrum is normalized relative to  $1280\text{\AA}$ . *Bottom Panel:* Examples of mean spectra of four quasar classes showing how the mean spectra from the top panel can be decomposed into four distinct classes. We generate these mean quasar spectra by classifying the PCA eigenvalues into four distinct classes using a Gaussian Mixture Model. The primary difference between different classes are the Ly- $\alpha$  and CIV emission strengths. The slope of the continua also show small change blueward of Ly- $\alpha$  emission between different classes. The vertical dotted lines mark the position of prominent emission features in the quasar continua. All the spectra are normalized relative to  $1280\text{\AA}$ .

the  $F(z_{\text{Ly-}\alpha})$  values with replacement 200 times. In each iteration, we compute a sigma clipped ( $\langle F(z_{\text{Ly-}\alpha}) \rangle$ ) as described in the previous step. We measure the final  $\langle F(z_{\text{Ly-}\alpha}) \rangle$  as the mean of these 200 bootstrapped estimates. We estimate the uncertainty on  $\langle F(z_{\text{Ly-}\alpha}) \rangle$  as the 16th and 84th percentile of the bootstrapped mean estimates,

which should account for sample variance, bad pixel contamination, and metal line contamination uncertainties.

- As the final step, we apply prescriptions to correct for metal line contamination as described below. We follow the methods of metal line contamination removal process discussed in Schaye et al.

(2003) and Kirkman et al. (2005) and then compute the corrected effective optical depth, and compare results in the Section 3.5.

## 4 RESULTS

### 4.1 Predicting Quasar Continua on $z < 1$ HST-COS Spectra

In this section we will describe the performance of both our PCA and iQNet deep learning neural network in predicting the UV continua of  $z < 1$  HST-COS quasars.

#### 4.1.1 PCA Performance

We first discuss the quasar continuum *reconstruction* performance of our PCA models over  $1020\text{\AA} \leq \lambda_{\text{rest}} \leq 1600\text{\AA}$  and compare them with the PCA reconstruction models in Suzuki et al. (2005) and Pâris et al. (2011), respectively. We apply the PCA reconstruction models on the quasar spectra with their full set of corresponding principal components, in the wavelength range ( $1020\text{\AA} \leq \lambda_{\text{rest}} \leq 1600\text{\AA}$ ). We stress that this method cannot be used to predict the true continuum blueward ( $1020\text{\AA} \leq \lambda_{\text{rest}} \leq 1216\text{\AA}$ ) of Ly- $\alpha$  emission, and discuss this in the context of PCA *reconstruction* performance only.

We gauge the performance of all these models with the testing quasar spectra, which are not used by any of the models to construct the PCA. This use of the blind testing sample was not used in neither Suzuki et al. (2005) nor Pâris et al. (2011), and the PCA model performance was tested on the same sample with which the original PCA models were constructed. We avoid this circularity to have a fair comparison between different models. Figure 6 shows a testing quasar spectrum, which is not used in the construction of PCA. Only our PCA model with the standardization process closely resembles the quasar continuum. Other PCA prediction models manage to predict Ly- $\alpha$  emission peak but cannot accurately predict the continuum in the regions with no emission lines. This demonstrates the reason why the standardization process is necessary to properly scale down the dominant features like Ly- $\alpha$  and CIV.

We quantify the PCA performance in reconstructing the quasar continua with the absolute fractional flux error (AFFE) as defined in equation 2 for the full testing sample and summarize the results in Table 2 for PCA reconstruction models. It is evident that the PCA model with the standardization process obtains the lowest AFFE and has two times lower AFFE as compared to Suzuki et al. (2005) and four times lower than Pâris et al. (2011) models. This is mainly because we implement the standardization process. The standardization process is a necessary step as PCA methods are sensitive to dominant features in the data set and can easily *overfit* the data if the dominant features are not properly scaled.

We further use these PCA models to *predict* the quasar continua blueward of Ly- $\alpha$  emission. In this case, the PCA model only utilizes the quasar spectra in the range  $1216\text{\AA} \leq \lambda_{\text{rest}} \leq 1600\text{\AA}$  and predicts the continuum in the range of  $1020\text{\AA} \leq \lambda_{\text{rest}} \leq 1216\text{\AA}$ . This method can be used to predict the quasar continuum in the Ly- $\alpha$  forest region at high redshift. We again only use the testing data set to make an independent assessment of all PCA prediction models. We compute the AFFE as the evaluation metric for the full testing sample. Table 3 shows that our PCA prediction model with the standardization process outperforms all other PCA-based models and predicts the underlying continua more accurately and with less bias on the testing quasar spectra. In the continuum prediction scenario, compared to the reconstruction case, our PCA with the standardization process surpasses other PCA models by lowering AFFE by approximately

PCA Reconstruction Model				
Model Name	Training Set Median	Mean	Testing Set Median	Mean
Suzuki PCA <sup>(a)</sup>	N/A	N/A	0.0593	0.0685
Paris PCA <sup>(a)</sup>	N/A	N/A	0.1180	0.1130
PCA (This work)	0.0668	0.0869	0.0663	0.0700
PCA+S <sup>(b)</sup> (This work)	0.0323	0.0352	0.0345	0.0364

**Table 2.** Absolute Fractional Flux Error (AFFE) on reconstructed continua of  $z \sim 0.2$  HST-COS training and testing 1-D spectra. <sup>(a)</sup>AFFE are not available for Suzuki et al. (2005) and Pâris et al. (2011) as the training set is used to construct these PCA models. The performances of these PCA-based models are evaluated only on the testing quasar spectra since they all have not used the testing data. <sup>(b)</sup>PCA+S represents our PCA model after applying the standardization process.

PCA Prediction Model				
Model Name	Training Set Median	Mean	Testing Set Median	Mean
Suzuki's PCA	N/A	N/A	0.0861	0.0951
Paris's PCA	N/A	N/A	0.1210	0.1290
PCA+S (This work)	0.0474	0.0590	0.0670	0.0628

**Table 3.** Absolute Fractional Flux Error of *predicted* continua of  $z < 1$  HST-COS training and testing quasar Spectra. AFFEs of training set are not available for Suzuki et al. (2005) and Pâris et al. (2011) as the training set is used to construct these PCA models. The performances of PCA-based models are evaluated only on the testing quasar spectra as the testing sample is blind to the PCA construction process. PCA+S represents our PCA model after the data standardization process. Clearly PCA+S model gives the best performance.

25%–50%. In all cases, we demonstrate that the standardization process is a necessary pre-processing step before model training.

#### 4.1.2 iQNet deep learning performance

Even though our PCA-based model outperforms other traditional PCA-based models, the PCA model itself does not learn anything from the training continua but decomposes a quasar continuum redward of Ly- $\alpha$  emission line to the corresponding eigenvectors in the training eigenspace and performs weighted superposition with weights of principal components. In other words, the researched models are all biased to the specific training data and are not robust to unseen testing quasar continua if the input to models is not properly standardized and normalized. Figure 7 shows that the PCA *prediction* model cannot predict the testing continuum correctly because it has never seen the testing continuum and has no learning ability to adapt and interpret the part of the spectrum redward of Ly- $\alpha$  transition. The PCA transformation matrix is only used to interconnect two PCA models, one for the part of continuum redward of Ly- $\alpha$  line ( $[1216, 1600]\text{\AA}$ ) and the other for whole continuum ( $[1020, 1600]\text{\AA}$ ). Therefore, the traditional PCA-based *prediction* models cannot generalize robustly well on unseen quasar continua, which is the reason why such models perform well only on their corresponding training quasar continua.

Another issue with PCA-based models in blindly predicting the blue side of Ly- $\alpha$  emission line is that we need to fit a continuum on the red-side of Ly- $\alpha$  first before applying PCA prediction models. PCA-based models cannot work directly with the quasar spectra but



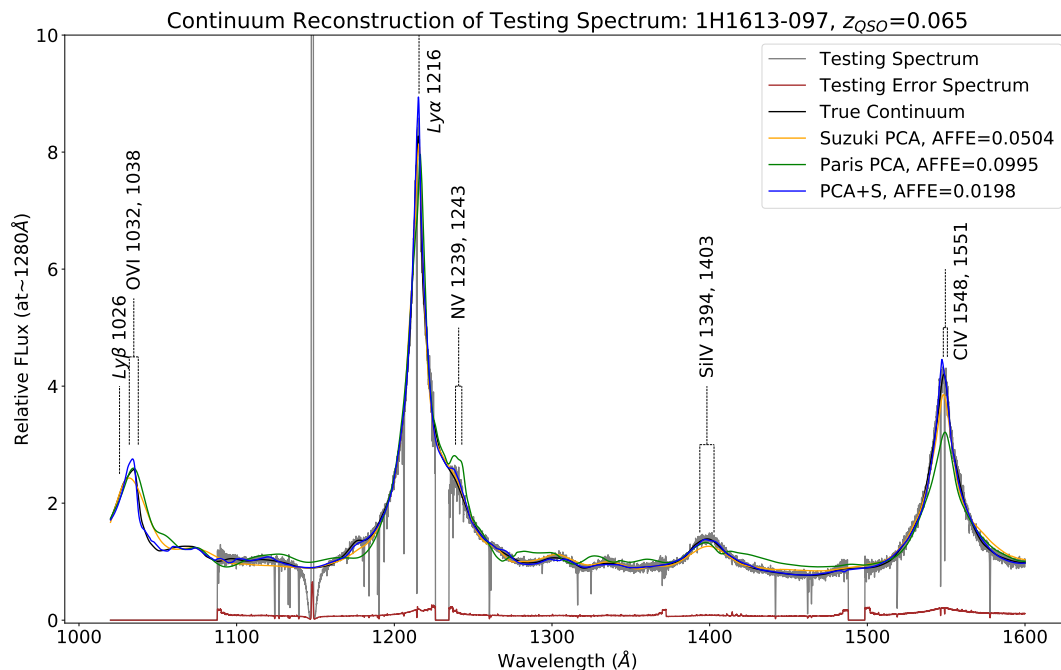


**Figure 6.** PCA reconstruction model comparison. The background testing spectrum and its corresponding ground truth continuum are shown in grey and black, respectively. The reconstructed continuum by Suzuki et al. (2005) is shown in orange and the reconstructed continuum by Pâris et al. (2011) in green. Our PCA reconstructed continuum with Standardization-Normalization is shown in blue. Other works fail to reconstruct the quasar continuum and have higher absolute fractional flux error (AFFE) (shown in legend) due to the lack of standardization process.

need human intervention to fit a spline curve and mask out absorption/emission lines before predicting the quasar continua. Different curve-fitting techniques may result in additional uncertainty in each spectrum that is ready to be fed into the model for the prediction of the whole continuum requiring researchers' inspection.

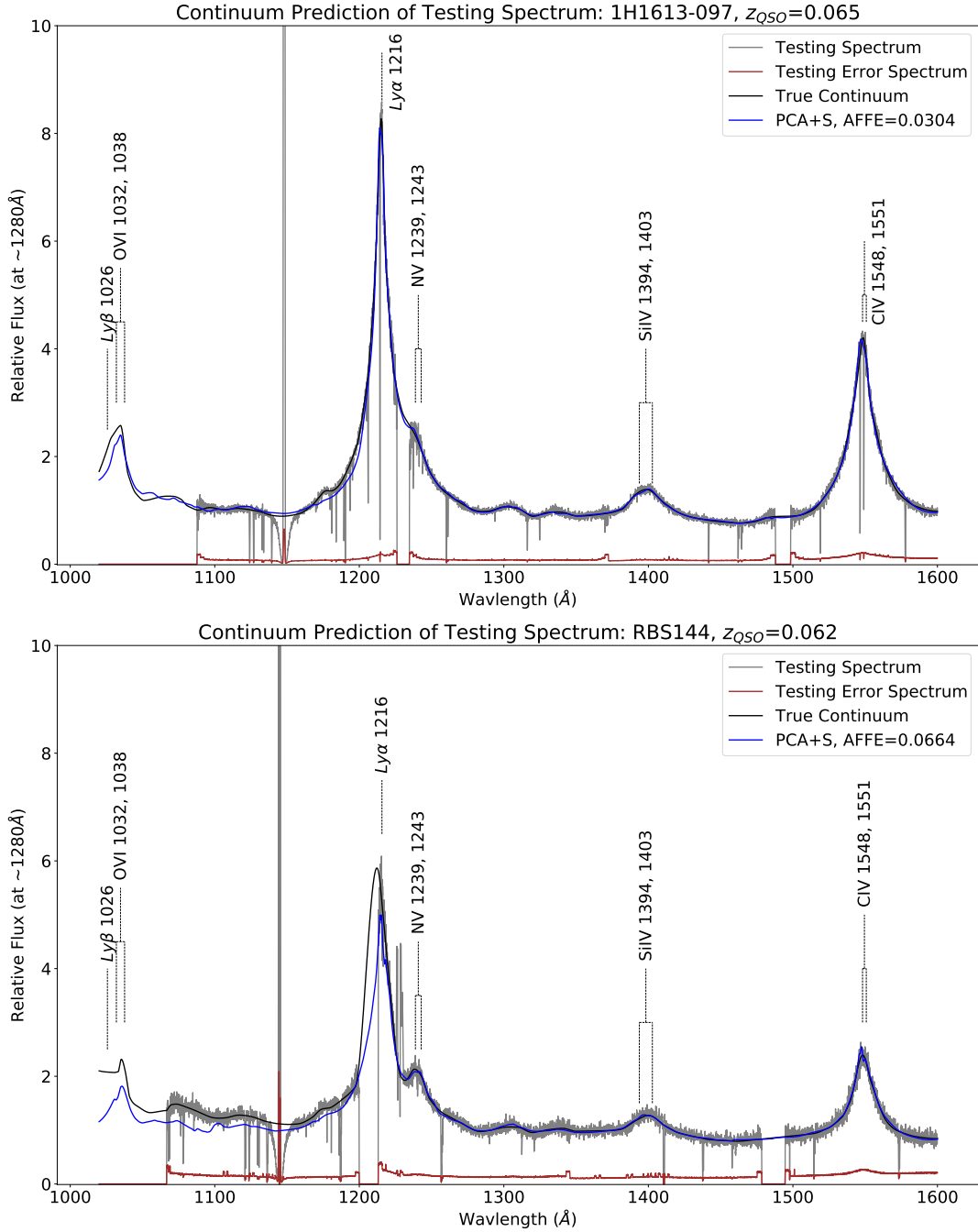
To reduce the amount of human inspection and to use the full information matrix that exists in each spectral pixel in predicting the quasar continuum, we apply the iQNet model directly on the quasar spectra and build a pipeline to automate the entire process. In the iQNet prediction model, the network takes a raw 1-D quasar spectrum within  $1216\text{\AA} < \lambda_{\text{rest}} \leq 1600\text{\AA}$  as input, and predicts the quasar continuum for the wavelength range  $1020\text{\AA} < \lambda_{\text{rest}} \leq 1600\text{\AA}$  as the output.

Table 4 presents the AFFE of both training and testing quasar spectra using iQNet. The median AFFE of predicted training continua is around 1.3%, which indicates that neural network can replicate our hand-fit continua with approximately 1% error, whereas the traditional PCA-based methods cannot achieve such low AFFE. More importantly, the iQNet has enhanced the performance on predicting the testing spectra and is able to generate a quasar continuum with only approximately 4% to 5% AFFE given a quasar spectrum that our model has not seen or trained. The additional advantage of the proposed iQNet model is that it is able to easily handle quasar spectra with missing data. Figures 8 and 9 demonstrate that the iQNet manages to predict a continuum close to the true continuum even though there are missing spectra within the wavelength range from  $1020\text{\AA}$  to  $1600\text{\AA}$ .

Figure 8 shows an example of the training spectrum comparing our PCA model and iQNet model. The iQNet is able to capture the emission features, denoise the spectra, and generate a smooth continuum by minimizing the AFFE between the predicted continuum and the ground truth continuum. The main advantage of applying

a deep learning model instead of the traditional PCA model is to minimize the loss function and monitor the AFFE during the training process. The traditional PCA models are linear transformations, whereas the neural networks are non-linear transformations. Therefore, the neural networks have better generalization ability than traditional PCA models. By monitoring the AFFE of the model prediction, the model learns and updates its weights to generate outputs as close to the ground truth as possible.

Evaluating a model performance on a training data set is not sufficient because the model has seen the training data and there is a chance that the same model may over-fit the training data set in order to obtain a low error or high accuracy. Therefore, we keep a testing set of quasar spectra that the model has never used. We train the neural network by minimizing its loss function but at the same time keeping the AFFE as low as possible. Figure 9 demonstrates two different quasar spectra in the testing set. In both cases, the results generated from iQNet outperforms the PCA model. The iQNet prediction generates moderately higher Ly- $\alpha$  emission than the ground truth, but the whole continuum traces the ground truth continuum successfully, whereas the PCA prediction fails to predict the continuum on the blue side of Ly- $\alpha$ . Even for a spectrum without strong emission features (e.g. Ly- $\alpha$  and CIV) the iQNet model is able to successfully generate a continuum correctly (Figure 9, bottom panel). The PCA-based prediction model, on the other hand, fails to predict the continuum at regions where there should have been emissions shown in the quasar spectrum. The fluctuation in the PCA prediction shows that the PCA extracts emissions as important and representative features, and the superposition of different principal components cannot fit a constant continuum at Ly- $\alpha$ .



**Figure 7.** PCA predictions of quasar continuum blueward of Ly- $\alpha$  transition on two  $z < 1$  HST-COS testing quasar spectra. The HST-COS testing spectra and the corresponding ground truth continua are shown in grey and blue, respectively. The predicted continua of our PCA-based prediction model with standardization is shown in blue. Top panel shows an example of a good prediction of the quasar continuum and the bottom panel show a bad prediction of the quasar continuum highlighting the shortcomings of all PCA based continuum prediction methods.

#### 4.2 Predicting Quasar Continuum on $2 < z \leq 5$ SDSS Spectra

In this section, we present results of quasar continuum predictions when we apply the PCA+S prediction model and the deep learning iQNet model to 3196  $2 < z \leq 5$  quasar spectra from SDSS DR16 Release (Ahumada et al. 2019). The fully trained deep learning method, iQNet, takes 3.379 seconds to successfully predict the 3196 selected SDSS 1D spectra (about 945 predictions per second). We ran the network on Google Colab without GPU or TPU enabled. This

is three times faster than the PCA+S model on the same architecture. The PCA+S needs 10.19 seconds to predict the 1d spectra, which is equivalent to making about 313 predictions per second.

Figure 10 presents six SDSS quasar spectra and their corresponding predicted continua based on PCA+S prediction model (blue line) and iQNet model (red line) within  $2 < z \lesssim 5$ . The PCA+S prediction model consistently overestimates the Ly- $\alpha$  and CIV emission peaks in all these spectra whereas the iQNet model successfully predicts those emission features. In addition, the iQNet

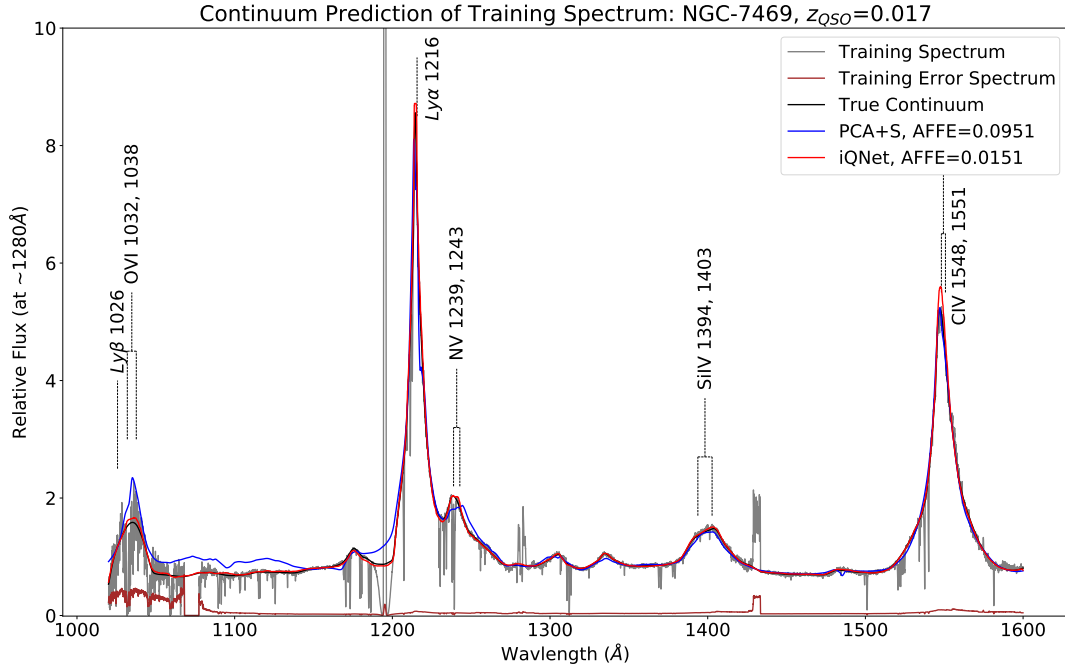


**Figure 8.** Example of an HST-COS training spectrum and its corresponding predicted continua with PCA prediction model and iQNet network. AFFEs are shown at the top. The training spectrum and its corresponding ground-truth continuum are shown in grey and black, respectively. The PCA Predicted Continuum in blue cannot predict the quasar continuum correctly blueward of Ly- $\alpha$  emission due to its limited extrapolation ability. The predicted continuum from our neural network in red almost completely overlaps the ground truth continuum.

**Table 4.** Absolute Fractional Flux Error of Predicted Continuum on HST Training and Testing Quasar Spectra.

Model Name	Training Set		Testing Set	
	Median	Mean	Median	Mean
PCA+S (This work)	0.0474	0.0590	0.0670	0.0628
iQNet (This work)	0.0131	0.0215	0.0417	0.0514

model is also better at adapting and predicting the full continuum even if there are no strong emission features redward of Ly- $\alpha$  emission in the spectrum (second row in Figure 10). As the performance of the iQNet network is superior to the traditional PCA based methods, we will only use the iQNet predicted continuum for the next analysis.

### 4.3 Evolution of Mean Transmitted Flux of the IGM

We use the iQNet predicted quasar continuum to estimate the mean transmitted flux ( $\langle F(z_{\text{Ly-}\alpha}) \rangle$ ) in the Ly- $\alpha$  forest region  $2 < z \lesssim 5$ . Following the steps in Section 3.5. We calculate  $\langle F(z_{\text{Ly-}\alpha}) \rangle$  in the rest-frame wavelength range  $[1080, 1160]\text{\AA}$  to account for contribution only from the Ly- $\alpha$  forest region.

The sample of SDSS spectra presents a large statistical sampling of the Ly- $\alpha$  forest region. Figure 11 illustrates the corresponding path length distribution of all the quasar 1-D spectral pixels in the Ly- $\alpha$  forest. Our sample covers the full redshift range  $1.96 < z_{\text{Ly-}\alpha} < 4.92$  with a mean  $\langle z_{\text{Ly-}\alpha} \rangle = 3.12$  and standard deviation of 0.618.

We compute the transmitted flux values and the corresponding effective optical depth values in the Ly- $\alpha$  forest region following the steps discussed in Section 3.5. Figure 12 shows distribution of

$F(z_{\text{Ly-}\alpha})$  in each redshift bin of interest. We can clearly see that the peak of the distribution shifts from  $\langle F(z_{\text{Ly-}\alpha}) \rangle > 0.9$  at  $z \sim 2$  to  $\langle F(z_{\text{Ly-}\alpha}) \rangle \sim 0.2$  at  $z \sim 5$ . These measurements are quantified and presented in Figure 13 as blue circles. The left panel shows the evolution of  $\langle F(z_{\text{Ly-}\alpha}) \rangle$  with redshift and the right panel shows the evolution of  $\tau_{\text{eff}}$ . The uncertainties are 16th and 84th percentiles of the bootstrapped mean distribution, computed from in each panel of Figure 12. We see a clear trend of smoothly declining  $\langle F(z_{\text{Ly-}\alpha}) \rangle$  with redshift.

These measurements are robust and more direct measurement of  $\tau_{\text{eff}}$  compared to literature results, as we are making no assumptions regarding the ionizing history of the Universe, and the most uncertain element of this measurement, the quasar continua, are estimated at  $z \sim 0.2$ . However, the secondary effects of contamination from the intervening line of sight metal absorption lines remain. These metal absorption line systems can arise from foreground CGM or IGM gas (Schaye et al. 2003; Steidel et al. 2010; Bordoloi et al. 2011; Zhu & Ménard 2013; Cooper et al. 2019). Our sigma clipping approach will account for some metal line contamination but it is not sufficient to get rid of all the contamination. To correctly measure  $\tau_{\text{eff}}$ , we need to remove the impact of these metal absorption line systems in the Ly- $\alpha$  forest, even though this in itself is a small effect (6-8%, Faucher-Giguère et al. 2008). We apply the methods discussed in Schaye et al. (2003) and Kirkman et al. (2005), and Figure 13 shows how the metal line corrections affect the mean transmitted flux as well as the effective optical depth. In Figure 13, the red and green points show how each metal absorption line correction prescription impacts the evolution of  $\tau_{\text{eff}}$  with redshift. Most impact is seen at  $z < 3.5$ , where  $\tau_{\text{eff}}$  changes by 9.88% for Schaye et al. (2003) metal line correction prescription and 9.61% for the Kirkman et al. (2005) metal line correction pre-

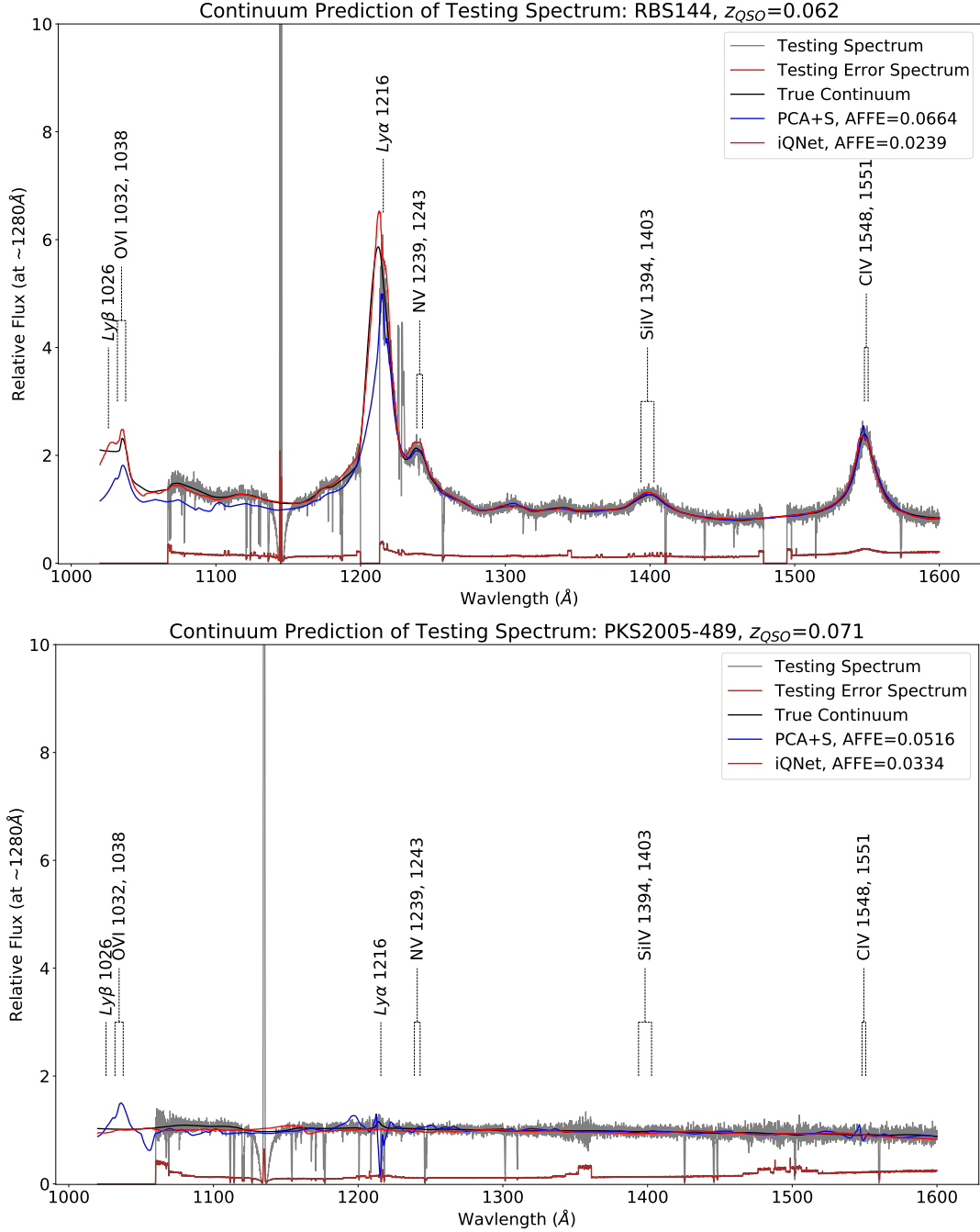


**Figure 9.** Examples of quasar continua prediction with PCA and iQNet network on two HST-COS testing quasar spectra. Top panel shows a quasar spectrum with strong Ly- $\alpha$  and CIV emission features and the bottom panel shows a quasar spectrum with no intrinsic emission line features. The testing spectra and the corresponding ground truth continua are shown in grey and black, respectively. The PCA Predicted Continuum (blue line) cannot predict the continua blueward of Ly- $\alpha$  emission correctly owing to its limited extrapolation ability. The predicted continua from iQNet (red line) almost overlap the ground truth continua.

scription. These values as well as the raw  $\langle F(z_{\text{Ly-}\alpha}) \rangle$  without metal line correction are tabulated in Table 5.

We quantify the evolution of  $\tau_{\text{eff}}$  by fitting a power law of a functional model

$$\log \tau_{\text{eff}} = b + m \log(1 + z_{\text{Ly-}\alpha}) \quad (6)$$

to the three estimates of  $\tau_{\text{eff}}$ . The best fit model parameters are also shown in Table 6. Our fits show a smooth evolution of  $\tau_{\text{eff}}$  with redshift and we find no evidence of a "bump" at  $z = 3.2$ , in agreement with Becker et al. (2013) and Pâris et al. (2011). We find

that the slopes of the effective optical depth start to increase beyond redshift  $z = 3.2$ , which indicates that the evolution of effective optical depth is nonlinear. This is broadly consistent with other literature results, which we will discuss in the next section.

#### 4.4 Comparison with Literature

In this section, we present the  $\tau_{\text{eff}}$  measurements of previous studies from the literature, which characterized the evolution of  $\tau_{\text{eff}}$  with

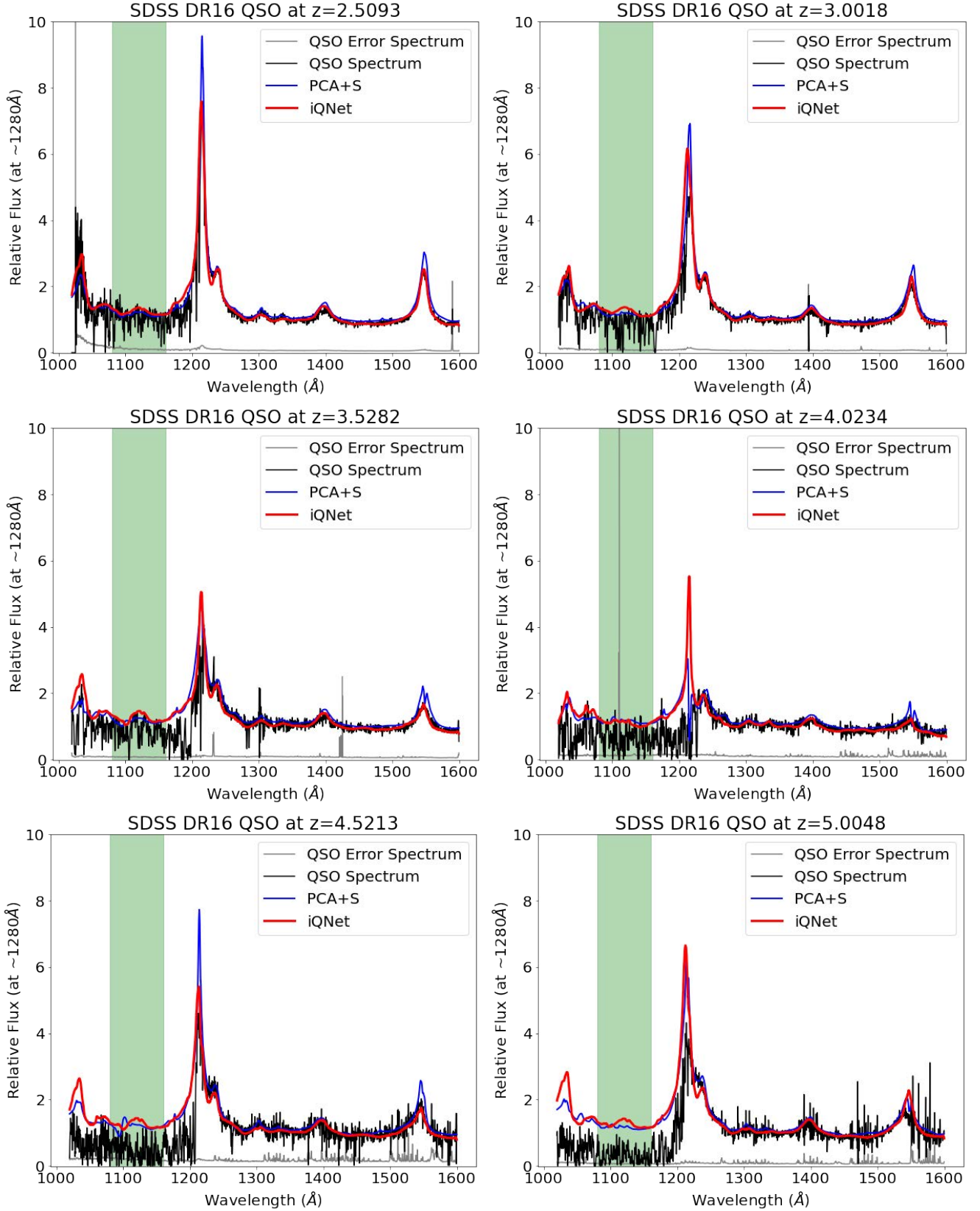


**Figure 10.** 1-D SDSS DR16 spectra of  $2 < z \leq 5$  quasars (black lines) along with their corresponding error spectra (gray lines) are presented in the quasar rest-frame. The PCA+S model fit (blue line) and deep neural network iQNet (red lines) predictions are also shown. For each case, iQNet outperforms the PCA+S model in predicting the overall 1-D quasar spectra. The mean transmitted flux is calculated within the green region shown in each panel.

**Table 5.** Effective optical depth values with and without metal line correction prescriptions. The first column,  $z_{\text{Ly-}\alpha}$ , describes the mean Ly- $\alpha$  redshift where the effective optical depth,  $\tau_{\text{eff}}$ , computed. The second column shows the raw measurements of the effective optical depth without metal absorption line corrections. The third and the fourth columns show the optical depth with metal line correction prescriptions by Schaye et al. (2003) and Kirkman et al. (2005), respectively.

$z_{\text{Ly-}\alpha}$	Effective Optical Depth, $\tau_{\text{eff}}$		
	Raw Measurements	Metal Absorption Line Correction from	
		Schaye et al	Kirkman et al
2.019	$0.136^{+0.018}_{-0.017}$	$0.118^{+0.019}_{-0.018}$	$0.105^{+0.019}_{-0.018}$
2.104	$0.173^{+0.015}_{-0.015}$	$0.151^{+0.017}_{-0.017}$	$0.143^{+0.017}_{-0.017}$
2.199	$0.197^{+0.014}_{-0.014}$	$0.173^{+0.015}_{-0.015}$	$0.166^{+0.015}_{-0.015}$
2.300	$0.226^{+0.015}_{-0.014}$	$0.200^{+0.016}_{-0.016}$	$0.196^{+0.016}_{-0.016}$
2.400	$0.250^{+0.014}_{-0.014}$	$0.222^{+0.016}_{-0.016}$	$0.220^{+0.016}_{-0.016}$
2.500	$0.280^{+0.016}_{-0.015}$	$0.250^{+0.017}_{-0.016}$	$0.251^{+0.017}_{-0.016}$
2.600	$0.298^{+0.017}_{-0.017}$	$0.267^{+0.017}_{-0.018}$	$0.270^{+0.017}_{-0.018}$
2.700	$0.345^{+0.018}_{-0.018}$	$0.310^{+0.018}_{-0.018}$	$0.316^{+0.018}_{-0.018}$
2.801	$0.359^{+0.018}_{-0.018}$	$0.324^{+0.019}_{-0.019}$	$0.331^{+0.019}_{-0.019}$
2.900	$0.403^{+0.019}_{-0.020}$	$0.366^{+0.020}_{-0.020}$	$0.376^{+0.020}_{-0.020}$
3.001	$0.431^{+0.020}_{-0.020}$	$0.393^{+0.020}_{-0.020}$	$0.404^{+0.020}_{-0.020}$
3.101	$0.462^{+0.021}_{-0.021}$	$0.423^{+0.021}_{-0.021}$	$0.435^{+0.021}_{-0.021}$
3.200	$0.494^{+0.021}_{-0.022}$	$0.454^{+0.022}_{-0.022}$	$0.468^{+0.022}_{-0.022}$
3.301	$0.537^{+0.023}_{-0.023}$	$0.496^{+0.023}_{-0.023}$	$0.511^{+0.023}_{-0.023}$
3.398	$0.581^{+0.024}_{-0.025}$	$0.539^{+0.024}_{-0.025}$	$0.556^{+0.024}_{-0.025}$
3.502	$0.632^{+0.025}_{-0.025}$	$0.588^{+0.025}_{-0.024}$	$0.607^{+0.025}_{-0.024}$
3.599	$0.697^{+0.027}_{-0.028}$	$0.651^{+0.027}_{-0.027}$	$0.672^{+0.027}_{-0.027}$
3.700	$0.733^{+0.027}_{-0.028}$	$0.688^{+0.027}_{-0.027}$	$0.709^{+0.027}_{-0.027}$
3.797	$0.757^{+0.028}_{-0.027}$	$0.712^{+0.027}_{-0.027}$	$0.733^{+0.027}_{-0.027}$
3.898	$0.816^{+0.029}_{-0.028}$	$0.770^{+0.028}_{-0.028}$	$0.792^{+0.028}_{-0.028}$
3.999	$0.885^{+0.030}_{-0.029}$	$0.838^{+0.029}_{-0.029}$	$0.862^{+0.029}_{-0.029}$
4.096	$0.973^{+0.031}_{-0.032}$	$0.925^{+0.030}_{-0.031}$	$0.950^{+0.030}_{-0.031}$
4.196	$1.024^{+0.031}_{-0.032}$	$0.976^{+0.030}_{-0.031}$	$1.001^{+0.030}_{-0.031}$
4.297	$1.045^{+0.033}_{-0.033}$	$1.000^{+0.032}_{-0.032}$	$1.023^{+0.032}_{-0.032}$
4.395	$1.076^{+0.034}_{-0.033}$	$1.033^{+0.033}_{-0.032}$	$1.054^{+0.033}_{-0.032}$
4.495	$1.205^{+0.037}_{-0.037}$	$1.160^{+0.036}_{-0.036}$	$1.184^{+0.036}_{-0.036}$
4.597	$1.325^{+0.033}_{-0.033}$	$1.279^{+0.032}_{-0.032}$	$1.304^{+0.032}_{-0.032}$
4.684	$1.417^{+0.041}_{-0.041}$	$1.372^{+0.040}_{-0.040}$	$1.396^{+0.040}_{-0.040}$
4.795	$1.534^{+0.026}_{-0.025}$	$1.490^{+0.026}_{-0.025}$	$1.513^{+0.026}_{-0.025}$
4.882	$1.617^{+0.034}_{-0.035}$	$1.575^{+0.033}_{-0.034}$	$1.598^{+0.033}_{-0.034}$

redshift. We compare our  $\tau_{\text{eff}}$  measurements with those reported in Faucherâ&Giguâ&re et al. (2008), Becker et al. (2013), and Pâris et al. (2011) respectively.

Figure 14, top left panel shows  $\tau_{\text{eff}}$  evolution as a function of redshift from Faucherâ&Giguâ&re et al. (2008) as black squares. Faucherâ&Giguâ&re et al. (2008) directly measured the effective optical depth in the redshift range  $2 \leq z \leq 4.2$  using 86 quasar spectra from moderate resolution Keck/ESI, and high-resolution Keck/HIRES, and magellan/MIKE spectrographs. They used the

peak flux in the Ly- $\alpha$  forest regions as their continuum estimates and performed spline fitting to obtain the quasar continuum in the Ly- $\alpha$  forest region. They further corrected their continuum estimates to correct for underestimating the true quasar continuum using mock spectra from theoretical models. They also accounted for intervening metal absorption lines from the IGM and corrected for these biases. Our  $\tau_{\text{eff}}$  measurements are shown as green circles in Figure 14 and the best fit  $\tau_{\text{eff}}$  profile is shown as the green band. These estimates are broadly consistent with Faucherâ&Giguâ&re



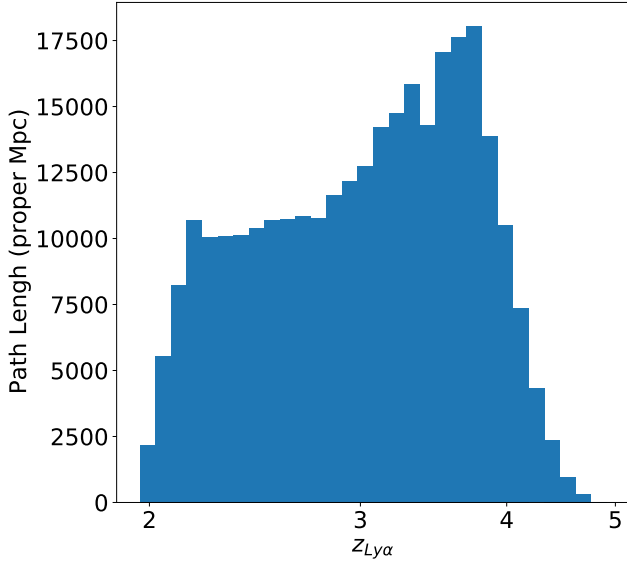


**Figure 11.** Proper path length distribution of Ly- $\alpha$  absorption, with  $\delta z_{\text{Ly-}\alpha} = 0.1$  interval, of the  $\sim 3200$  quasar spectra used from the SDSS survey. The spectra gives a near uniform coverage of the Ly- $\alpha$  forest up to  $z \sim 5$ .

**Table 6.** Model parameters of fitting power-law curves of three models in Equation 6. The fitting curves among all models are plotted in Figure 14.

Model Name	$b$	$m$
Raw Measurements	$-2.421^{+0.021}_{-0.023}$	$3.402^{+0.032}_{-0.031}$
Schaye Correction	$-2.564^{+0.022}_{-0.023}$	$3.571^{+0.032}_{-0.031}$
Kirman Correction	$-2.567^{+0.022}_{-0.022}$	$3.587^{+0.031}_{-0.031}$

et al. (2008) over the range  $2 < z_{\text{Ly-}\alpha} \leq 3.5$ . The difference beyond  $z_{\text{Ly-}\alpha} > 3.5$  is primarily owing to the fact that their continuum bias correction at higher redshift is too large. Whereas, in this work, we are directly estimating the quasar continuum from  $z \sim 0$  quasars, and do not require any correction to continuum estimates. In addition, we do not find the "dip" feature identified by Faucher-Giguère et al. (2008) at  $z \sim 3.2$ . Our findings are consistent with those of Pâris et al. (2011) and Becker et al. (2013) that this feature is not observed for more precise measurements of  $\tau_{\text{eff}}$ .

We proceed to compare our  $\tau_{\text{eff}}$  measurements with results from Pâris et al. (2011) and Becker et al. (2013). Since our  $\tau_{\text{eff}}$  measurements are only from SDSS DR16 quasar spectra, we restrict our comparison to these two studies. We refer the readers to Becker et al. (2013) for a detailed comparison of other studies of  $\tau_{\text{eff}}$  evolution (e.g. Bernardi et al. 2003; McDonald et al. 2005; Dall’Aglio et al. 2009).

Figure 14, top right panel shows that the results from Becker et al. (2013) (gold diamonds). These are the most consistent results with our  $\tau_{\text{eff}}$  estimates over the whole redshift range  $2.5 \leq z_{\text{Ly-}\alpha} < 5$ . Becker et al. (2013) applied the method of composite quasar spectra on SDSS DR7 to measure the mean transmitted flux in the Ly- $\alpha$  forest over  $2 < z < 5$ . They combined 6065 quasar spectra into 26 composites with mean redshift at  $2.25 \leq z_{\text{composites}} \leq 5.08$ , and then corrected their measurements with data from Faucher-Giguère et al. (2008) at  $z \leq 2.5$ , how-

ever they did not apply metal absorption line correction in their work, because the flux ratio measurement in their composite spectra is an equivalent method to reduce the metal line contamination in the Ly- $\alpha$  forest region. Indeed this is a valid approach, as our  $\tau_{\text{eff}}$  estimates after metal line correction are more or less consistent with that from Becker et al. (2013). Our  $\tau_{\text{eff}}$  measurements slightly differ from these measurements over  $2 \leq z < 2.5$ . This is mainly owing to the fact that Becker et al. (2013) assumes that the true quasar continuum without contamination from Ly- $\alpha$  forest can be measured in this redshift range, whereas we are estimating the quasar continuum with  $z \sim 0.2$  quasar spectra. Therefore, the Becker et al. (2013) composite spectra may have some Ly- $\alpha$  forest contamination at  $z_{\text{Ly-}\alpha} \sim 2$  and under-estimate the true continuum blueward of Ly- $\alpha$  transition. Otherwise, Becker et al. (2013)  $\tau_{\text{eff}}$  estimates are very close to our results after correcting for the metal absorption line contamination.

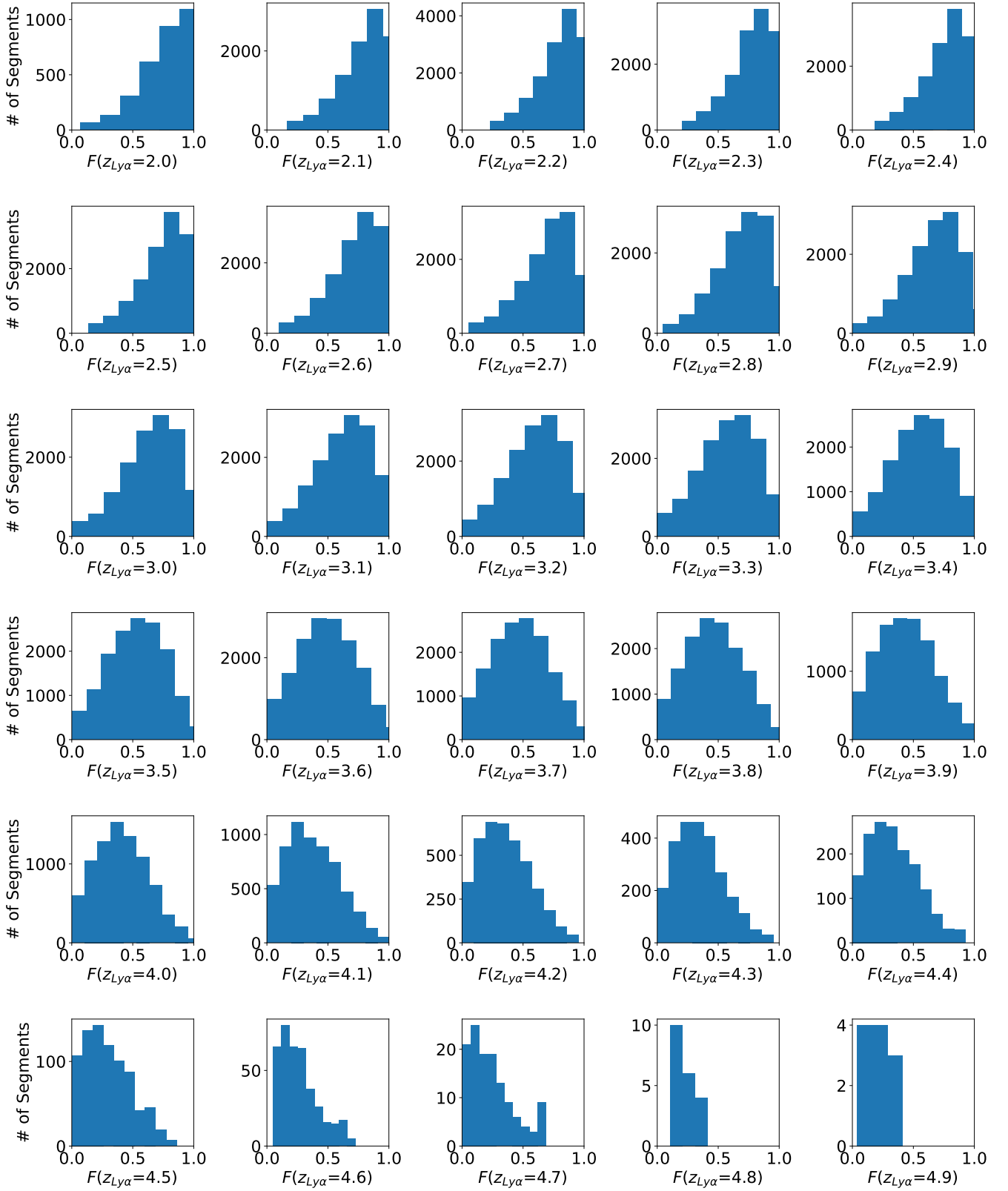
Lastly, we compare our results with those of Pâris et al. (2011) to compare the neural-network-based model results with that of a PCA-based model. Pâris et al. (2011) measured the mean transmitted flux by applying the PCA-prediction model on the quasar spectra in the SDSS DR7 to obtain the true quasar continua. They assumed that the true quasar continua blueward of the quasar Ly- $\alpha$  emission can be found by fitting a spline curve to the flux peaks in the Ly- $\alpha$  forest region at  $z \sim 3$ . Pâris et al. (2011) did not perform any metal absorption line correction or absolute scaling when computing the mean transmitted flux. We show the  $\tau_{\text{eff}}$  estimates from Pâris et al. (2011) as purple triangles in Figure 14, bottom panel. Their mean estimates of  $\tau_{\text{eff}}$  over the range  $3.7 < z_{\text{Ly-}\alpha} < 4.0$  are slightly higher than our measurements. These differences could be because of how the true continuum model was constructed. While we are using low redshift quasar spectra, Pâris et al. (2011) fitted the peaks of Ly- $\alpha$  forest region at higher redshift  $z_{\text{QSO}}$  where there are some Ly- $\alpha$  forest present. This method of fitting the peaks may be overestimating the true quasar continuum at  $z_{\text{QSO}}$ .

Figure 14 also shows the best fit power law evolution of  $\tau_{\text{eff}}$  as a function of redshift (green lines). Overall, the evolution of  $\tau_{\text{eff}}$  with redshift from literature are broadly consistent with our measurements. Our measurements suggest a smooth evolution of  $\tau_{\text{eff}}$  with redshift suggesting a more or less a smooth evolution of ionization and thermal state of the IGM. All subtle differences between these studies and our current measurements are mainly coming from the fact that we are estimating the most accurate quasar continuum blueward of Ly- $\alpha$  transition uncontaminated by Ly- $\alpha$  forest absorption.

## 5 CONCLUSIONS

In this paper, we introduce a novel deep learning approach, intelligent quasar continuum neural network (iQNet), to predict the quasar continuum in the rest frame wavelength range of  $1020\text{\AA} \leq \lambda_{\text{rest}} \leq 1600\text{\AA}$ . We train the iQNet model with high-resolution quasar spectra at low redshift  $z_{\text{QSO}} \sim 0.2$  from the Hubble Spectroscopic Legacy Archive (HSLA). Our flexible model can predict the quasar continua at any  $z_{\text{QSO}}$  for any arbitrary survey. We test the iQNet network performance with a testing sample of quasar spectra from HSLA and apply it to predict quasar continua of 3196 SDSS DR16 quasars at  $2 < z_{\text{QSO}} \leq 5$ . Our main findings are summarized below:

- Before we train a network or perform any PCA analysis, a standardization process of the data is necessary. This standardization process helps reduce model training bias and over-fitting.



**Figure 12.** Distribution of transmitted flux  $F(z_{Ly-\alpha})$  in 3-Mpc segment bins for different redshift bins. Each of the panels represents a redshift bin with width of  $\Delta z = 0.1$ . The mean transmitted flux in each bin continuously decreases with redshift. The  $\langle F(z_{Ly-\alpha}) \rangle$  and the associated uncertainties are computed by bootstrapping the transmitted flux distribution in each redshift bin.

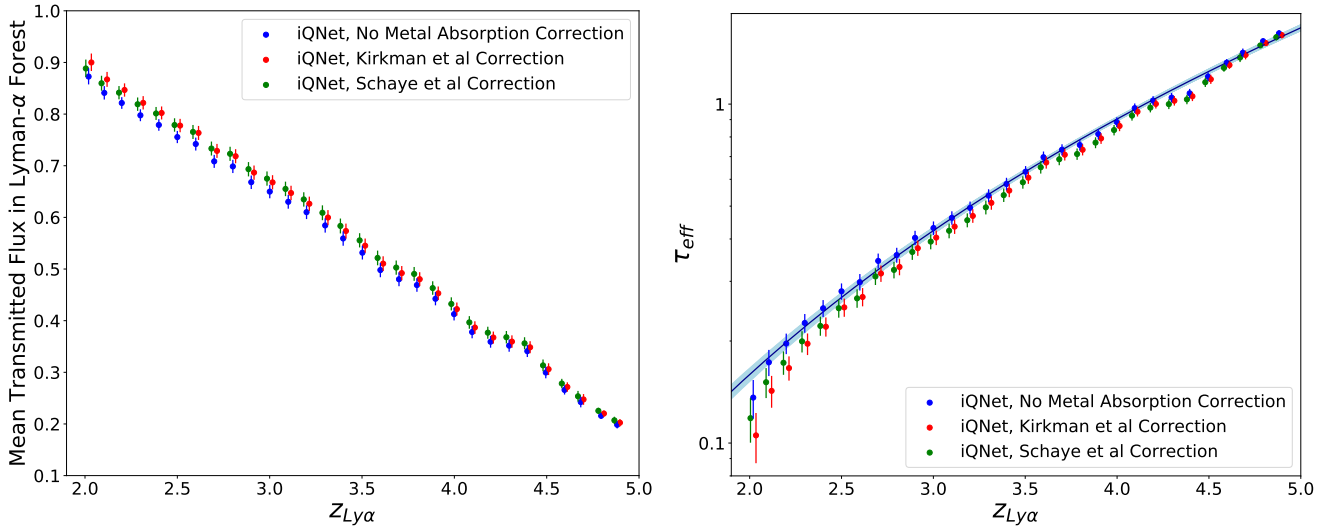


**Figure 13.** Comparison of Metal Absorption Correction methods. Left panel shows the mean transmitted flux in Ly- $\alpha$  forest with iQNet continuum predictions (blue points) and the metal line absorption corrections by Kirkman et al. (2005) (red points) and Schaye et al. (2003) (green points). Right panel demonstrates the corresponding effective optical depth to the iQNet predictions (blue points) with metal line absorption corrections by Kirkman et al. (2005) (red points) and Schaye et al. (2003) (green points). For better visualization, we uniformly shift  $z_{Ly-\alpha}$  by 0.015 to the left for the results corrected by Kirkman et al. (2005) method and 0.015 to the right for those by Schaye et al. (2003) method, respectively. The blue curve indicates the fitting function in Equation 6

In typical quasar spectra, the Ly- $\alpha$  and CIV emission lines are dominant features within the rest-frame wavelength range over  $1020\text{\AA} \leq \lambda_{rest} \leq 1600\text{\AA}$ . Any machine learning or PCA models will be biased towards those features if these two emissions are not properly scaled. This will result in biased model predictions for different quasar observations.

- We construct a PCA prediction model with a standardization process (PCA+S) on the quasar spectra and find that our model gives a mean AFFE (Equation 2) of 0.590 on training data and 0.0628 on testing data. Even though our PCA+S prediction model outperforms all other published PCA models, the generalizability of PCA+S is limited due to the lack of learning ability. The PCA prediction model cannot predict a constant-flux continuum, as we discuss in Figure 9, whereas the iQNet model can easily handle this scenario.

- We can characterize all quasar spectra into 4 distinct classes, using a GMM and the decomposed principal components. These classes are representative of all the quasars used for this work. The main differences among those 4 classes of quasar spectra are the emission strengths of the Ly- $\alpha$  and CIV features. We also find a smaller difference in the slope of the continua blueward of Ly- $\alpha$  emission.

- We use the PCA+GMM classes to create 11947 synthetic quasar spectra (12000 training spectra in total including 53 HSLA real quasar spectra). We inject strong ISM and HI absorption lines at random redshifts and change the S/N of the spectra to create a diverse range of training samples. We train The iQNet model on these 12000 training spectra with a binary cross-entropy loss function and AFFE monitoring over 40 minutes on the Google Colab platform with GPU enabled. We also add a standardization process and its corresponding inverse transformation process before the input layer of iQNet and after the output layer, respectively, to properly scale quasar continua after iQNet model prediction.

- We find that the iQNet model can achieve a median absolute fractional flux error 1.31% on the training data set at  $z \sim 0.2$ , which is approximately 3.6 times lower than our PCA prediction model

with the standardization process. Comparing with AFFE reports on training sets from other literature (AFFE  $\approx 6\%$  in Pâris et al. 2011, and AFFE  $\approx 9\%$  in Suzuki et al. 2005), our iQNet model outperforms all PCA prediction models based on the performance to predict the training data. In the blind testing set, the iQNet model outperforms all other PCA prediction models and achieves an AFFE 0.0417, which is approximately half the AFFE from Suzuki et al. (2005) PCA prediction model and only one-third of AFFE from Pâris et al. (2011) PCA. We find an AFFE 4.17% on the testing data set at  $z \sim 0.2$ .

- We ran the iQNet model on a standard Google Colab CPU architecture and it can predict about 945 high-resolution quasar continua per second, without utilizing GPU or TPU. This is almost three times faster than PCA prediction models that were run on the same hardware architecture. In addition, the usage of iQNet model does not require a fitted continuum of the redward of Ly- $\alpha$  emission of a quasar spectrum, but only needs a quasar spectrum with the proper standardization applied. This further reduces the processing time to generate a quasar continuum compared among other quasar continuum estimation techniques.

- We apply the iQNet model to predict the rest-frame quasar continua of  $3196 \leq z_{QSO} \leq 5$  quasars from the SDSS survey. We use these continua predictions to estimate the mean transmitted flux ( $\langle F \rangle$ ) and the corresponding effective optical depth ( $\tau_{eff}$ ) in the Ly- $\alpha$  forest region. We find that  $\tau_{eff}$  evolves smoothly with redshift and can be characterized by a power-law evolution as  $\tau_{eff} = 0.00273^{+0.000142}_{-0.000141} (1 + z_{Ly-\alpha})^{3.571^{+0.032}_{-0.031}}$ .

- Our  $\langle F \rangle$  estimates are broadly consistent with those reported in the literature although these works used different methods to measure  $\langle F \rangle$  (Faucher-Giguère et al. 2008; Pâris et al. 2011; Becker et al. 2013). Our approach is a more direct measurement of  $\langle F \rangle$  compared to other methods, as we are directly predicting the quasar continua (the most uncertain element of these measurements) from  $z \sim 0.2$  observations, where the impact of Ly- $\alpha$  forest is the least. This confirms that the iQNet model achieves accurate predictions of quasar continua at higher redshift  $2 < z_{QSO} \leq 5$ .

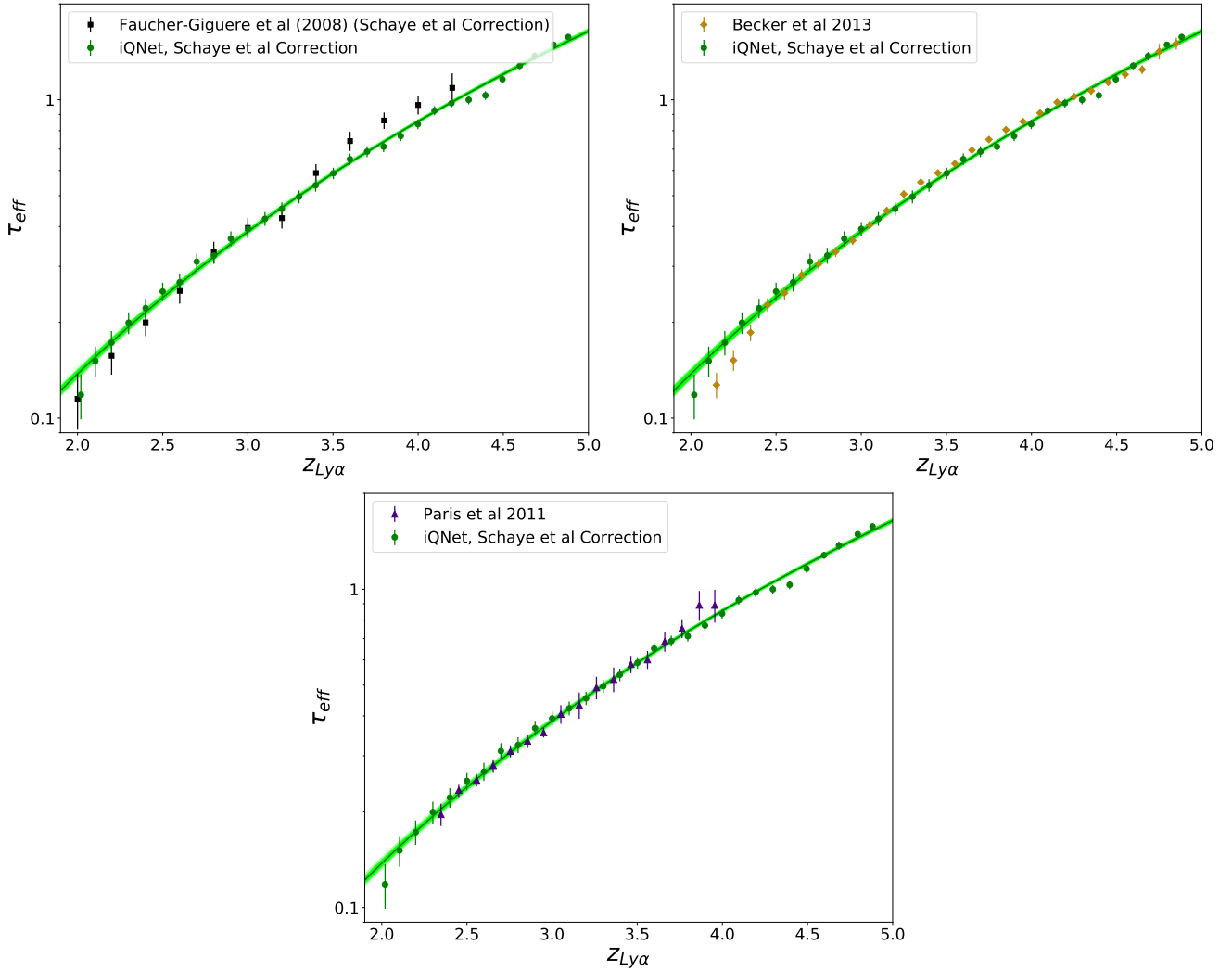


**Figure 14.** Comparison of our effective optical depth values,  $\tau_{\text{eff}}$ , with other published results. Top left panel shows our results along with the results from Faucher-Giguere et al. (2008) employing the Schaye et al. (2003) metal-line contamination correction. Top right panel shows our results and Becker et al. (2013). Bottom right shows the comparison between our measurements and Pâris et al. (2011). The green fitting curves represent the fitting function in Equation 6 with the best-fit parameters listed in Table 6.

Moreover, the architecture of our iQNet reveals a new approach to generate a quasar continuum, predict the continuum blueward of Ly- $\alpha$  emission at high redshift, and study the Ly- $\alpha$  forest. The number of neurons in each layer and the number of hidden layers in the neural network can be adapted to various quasar spectra and different instruments. Future studies may need to find another criterion, similar to the absolute fractional flux error, to evaluate the goodness of continuum fit and optimize the neural network models. Our iQNet proves that even the simplest vanilla neural network with fully-connected layers is able to generate quasar continua within an AFPE of 1% on a training set and that of 4% on a testing data set, far outperforming PCA based methods. Thus, the architectures of the convolutional variational autoencoder(ConvVAE) and the generative adversarial network(GAN) may be the next model structures that researchers would want to apply to quasar spectra because those neural networks have better nonlinear representation and generalization ability than neural networks with only fully-connected neurons. We will explore these options in future work as well as extend our work to  $z > 6$  quasars.

## ACKNOWLEDGEMENTS

This research has made use of the HSLA database, developed and maintained at STScI, Baltimore, USA, and Astropy,<sup>8</sup> a community-developed core Python package for Astronomy (Astropy Collaboration et al. 2013; Price-Whelan et al. 2018). We are extremely grateful to J. X. Prochaska, J. Chisholm, and J. Burchett for their careful reading of the draft and constructive comments and suggestions, that helped improve the paper.

## REFERENCES

- Abadi M., et al., 2015, TensorFlow: Large-Scale Machine Learning on Heterogeneous Systems, <http://tensorflow.org/>  
 Ahumada R., et al., 2019, The Sixteenth Data Release of the Sloan Digital Sky Surveys: First Release from the APOGEE-2 Southern Survey and Full Release of eBOSS Spectra (arXiv:1912.02905)

<sup>8</sup> <http://www.astropy.org>

- Astropy Collaboration et al., 2013, *A&A*, 558, A33
- Becker G. D., Bolton J. S., Haehnelt M. G., Sargent W. L. W., 2010, *Monthly Notices of the Royal Astronomical Society*, 410, 1096â–1112
- Becker G. D., Hewett P. C., Worseck G., Prochaska J. X., 2013, *Monthly Notices of the Royal Astronomical Society*, 430, 2067â–2081
- Bernardi M., et al., 2003, *AJ*, 125, 32
- Bolton J. S., Haehnelt M. G., Viel M., Springel V., 2005, *Monthly Notices of the Royal Astronomical Society*, 357, 1178â–1188
- Bordoloi R., et al., 2011, *ApJ*, 743, 10
- Bordoloi R., et al., 2014, *The Astrophysical Journal*, 796, 136
- Buitinck L., et al., 2013, in *ECML PKDD Workshop: Languages for Data Mining and Machine Learning*, pp 108–122
- Calinski T., Harabasz J., 1974, *Communications in Statistics-Simulation and Computation*, 3, 1
- Cen R., Miralda-Escudé J., Ostriker J. P., Rauch M., 1994, *ApJ*, 437, L9
- Chen H.-W., et al., 2018, *Monthly Notices of the Royal Astronomical Society*, 484, 431â–441
- Chollet F., et al., 2015, Keras, <https://keras.io>
- Cooper T. J., Simcoe R. A., Cooksey K. L., Bordoloi R., Miller D. R., Furesz G., Turner M. L., Bašados E., 2019, *The Astrophysical Journal*, 882, 77
- Croft R. A. C., Weinberg D. H., Katz N., Hernquist L., 1998, *The Astrophysical Journal*, 495, 44â–52
- Croft R. A. C., Weinberg D. H., Bolte M., Burles S., Hernquist L., Katz N., Kirkman D., Tytler D., 2002, *The Astrophysical Journal*, 581, 20â–52
- Dall'Aglio A., Wisotzki L., Worseck G., 2009, *arXiv e-prints*, p. arXiv:0906.1484
- Davies F. B., et al., 2018, *The Astrophysical Journal*, 864, 143
- FaucherâGiguere C., Lidz A., Zaldarriaga M., Hernquist L., 2008, *The Astrophysical Journal*, 673, 39â–51
- FaucherâGiguere C., Prochaska J. X., Lidz A., Hernquist L., Zaldarriaga M., 2008, *The Astrophysical Journal*, 681, 831â–855
- Flesch E. W., 2019, *The Million Quasars (Milliquas) Catalogue*, v6.4 (arXiv:1912.05614)
- Green J. C., et al., 2011, *The Astrophysical Journal*, 744, 60
- Hernquist L., Katz N., Weinberg D. H., Miralda-Escudé J., 1996, *The Astrophysical Journal*, 457
- Higley A. N., et al., 2020, in *American Astronomical Society Meeting Abstracts*. American Astronomical Society Meeting Abstracts. p. 219.03
- Hinshaw G., et al., 2013, *The Astrophysical Journal Supplement Series*, 208, 19
- Kingma D. P., Ba J., 2014, Adam: A Method for Stochastic Optimization (arXiv:1412.6980)
- Kirkman D., et al., 2005, *Monthly Notices of the Royal Astronomical Society*, 360, 1373â–1380
- Lee K.-G., Suzuki N., Spergel D. N., 2012, *The Astronomical Journal*, 143, 51
- McDonald P., Miralda-Escudé J., Rauch M., Sargent W. L. W., Barlow T. A., Cen R., 2001, *The Astrophysical Journal*, 562, 52â–75
- McDonald P., et al., 2005, *ApJ*, 635, 761
- Pâris et al., 2011, *A&A*, 530, A50
- Peeples M., et al., 2017, Technical report, The Hubble Spectroscopic Legacy Archive
- Prechelt L., 1996, in *Neural Networks: Tricks of the Trade*.
- Price-Whelan A. M., et al., 2018, *AJ*, 156, 123
- Rauch M., et al., 1997, *The Astrophysical Journal*, 489, 7â–20
- Reynolds D. A., 2009, *Encyclopedia of biometrics*, 741
- Schaye J., Aguirre A., Kim T., Theuns T., Rauch M., Sargent W. L. W., 2003, *The Astrophysical Journal*, 596, 768â–796
- Schwarz G., 1978, *The Annals of Statistics*, 6, 461
- Shull J. M., 2014, *The Astrophysical Journal*, 784, 142
- Songaila A., 2004, *The Astronomical Journal*, 127, 2598â–2603
- Steidel C. C., Erb D. K., Shapley A. E., Pettini M., Reddy N., Bogosavljević M., Rudie G. C., Rakic O., 2010, *The Astrophysical Journal*, 717, 289â–322
- Suzuki N., Tytler D., Kirkman D., O'Meara J. M., Lubin D., 2005, *The Astrophysical Journal*, 618, 592
- Tumlinson J., et al., 2013, *The Astrophysical Journal*, 777, 59
- Vincent P., Larochelle H., Lajoie I., Bengio Y., Manzagol P.-A., 2010, *J. Mach. Learn. Res.*, 11, 3371
- Werk J. K., et al., 2014, *The Astrophysical Journal*, 792, 8
- Zhou Y., Chellappa R., Vaid A., Jenkins B. K., 1988, *IEEE Transactions on Acoustics, Speech, and Signal Processing*, 36, 1141
- Zhu G., Ménard B., 2013, *ApJ*, 770, 130

This paper has been typeset from a  $\text{\LaTeX}$  file prepared by the author.